Chemical Geology 662 (2024) 122235

Contents lists available at ScienceDirect

Chemical Geology

journal homepage: www.elsevier.com/locate/chemgeo

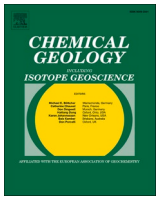

Effects of gamma(γ)-irradiation on the physicochemical properties and bioavailability of iron oxyhydroxides coprecipitated with varying concentrations of Na-alginate

Tarek Najem [a], Prachi Joshi [b], Andreas Kappler [b], Danielle Fortin [a,*]

[a] Department of Earth and Environmental Sciences, University of Ottawa, 25 Templeton St., K1N6N5 Ottawa, Ontario, Canada
[b] Geomicrobiology, Department of Geoscience, University of Tuebingen, Geschwister-Scholl-Platz, 72074 Tübingen, Germany

ARTICLE INFO

Editor: Dr. Hailiang Dong

Keywords:
Iron oxyhydroxides
Na-alginate
Co-precipitate
γ-Irradiation
Mössbauer spectroscopy
Bioavailability
Shewanella putrefaciens

ABSTRACT

This study investigated the impacts of γ-radiation at a final dose of 25 kGy on the physicochemical properties of a range of wet iron oxyhydroxides (2-line ferrihydrite, lepidocrocite, and goethite) synthesized in the presence of varying concentrations of the polysaccharide Na-alginate (starting solutions containing C/Fe ratios of 0, 0.5, 1.0, and 1.5). The degree of impact to the minerals was examined by chemical extractions, and various analytical techniques including XRD, FTIR-ATR, Mössbauer spectroscopy, and N_2 adsorption-desorption isotherms, as well as by assessing their bioavailability towards the model Fe(III) reducing bacteria *Shewanella putrefaciens* CN32. Across all the coprecipitates studied, it was found that γ-irradiation led to a substantial dissolution of Fe and the concomitant release of Fe(II) and alginate into solution. Despite this observation, the bulk mineralogy and crystallinity of the studied iron oxyhydroxides, as determined by XRD and FTIR-ATR, did not appear to change. However, analyses via Mössbauer spectroscopy (77 and 5 K) revealed that the crystallinity of the 2-line ferrihydrites increased post-irradiation. Moreover, among the minerals studied, the specific surface area and porosity decreased for only the post-irradiated 2-line ferrihydrite coprecipitates with a C/Fe ratio of 0.5 or 1.0. The bioreduction rates of the studied minerals and their irradiated counterparts did not significantly differ, whereas the extent of bioreduction of post-irradiated 2-line ferrihydrite coprecipitates (C/Fe 0.5, 1.0, and 1.5) exhibited a significant increase of up to 28%. In contrast, the extent of Fe reduction for select post-irradiated lepidocrocite (C/Fe 0.5) and goethite (C/Fe 1.5) coprecipitates was slightly higher than determined for their corresponding native controls. The observed differences in bioavailability between the native and irradiated coprecipitates were attributed to irradiation induced alteration of particle aggregation and coagulation as determined by particle size analyses and visual observations. In summary, the findings suggest that even a low total dose of 25 kGy, γ-radiation can lead to significant physicochemical changes in coprecipitates with relatively low organic matter content. Therefore, future research designed to investigate organic matter-Fe composite systems in natural samples should be cognizant of the potential effects of sterilization through γ-irradiation. These effects could potentially result in inaccurate over- or under- estimations of the bioavailability of Fe or organic matter, as well as the possible adsorption capacity of organic matter-Fe coprecipitates for contaminants.

1. Introduction

Sterilization of natural samples is essential for distinguishing biotic from abiotic reactions in laboratory experiments investigating the rate and extent of biogeochemical processes, and to prevent sample alteration during experimentation and storage (McNamara et al., 2003). From the range of available sterilization methods reported in the literature, apparently all come with a disadvantage. Autoclaving, for instance, can significantly alter the physicochemical properties of natural samples, including a decrease of surface area as a consequence of heat induced transformation of poorly crystalline Fe oxyhydroxide minerals into crystalline iron oxides as well as particle aggregation (Berns et al., 2008; Radloff et al., 2008; Zhao et al., 2017; Otte et al., 2018), and release of nutrients and organic matter (Salonius et al., 1967; Lotrario et al., 1995; McNamara et al., 2003; Berns et al., 2008; Buessecker et al., 2019). On the other hand, the application of chemical

* Corresponding author.
E-mail address: dfortin@uottawa.ca (D. Fortin).

https://doi.org/10.1016/j.chemgeo.2024.122235
Received 25 March 2024; Received in revised form 12 June 2024; Accepted 14 June 2024
Available online 17 June 2024

agents was reported to result in the increase of extractable of Fe(II) and Fe(III) (Buessecker et al., 2019; Layglon et al., 2020), as well as the chemical alteration of organic matter properties and trace metal behaviour (Wolf et al., 1989; Buessecker et al., 2019; Retelletti Brogi et al., 2019; Layglon et al., 2020). Moreover, the application of chemical agents may hinder the inoculation of sterilized samples with model microorganisms (Langley et al., 2009a; Langley et al., 2009c; Langley et al., 2009d).

Although autoclaving tends to be more commonly used due to its lower cost and ease of accessibility, sterilization by gamma(γ)-irradiation has been determined to be the most appropriate method by several studies (McNamara et al., 2003; Herbert et al., 2005; Berns et al., 2008; Borisover et al., 2016; Lees et al., 2018; Buessecker et al., 2019). Such preference is attributed to its effectiveness as a biocide that precludes the use of toxic chemicals, and the harsh pressure and heat treatments through autoclaving especially where repeated treatments are required (Wolf et al., 1989; Lensi et al., 1991; McNamara et al., 2003; Zhao et al., 2017). Typically, elimination of microbial activity is dose-dependent where up to 70 kGy or higher may be necessary to inactivate certain radio-resistant bacteria (McNamara et al., 2003). The mechanism of sterilization by γ-radiation proceeds via direct and indirect pathways (McNamara et al., 2003). The latter leads to production of the radiolysis products (e.g., $^{\bullet}OH$, e^{-}_{aq}, H_2O_2) from water that are also associated with the alteration of the physicochemical properties of natural samples (Plötze et al., 2003; Bank et al., 2008; Berns et al., 2008). Although some studies found no discernible changes in the physicochemical properties of natural or synthetic samples at doses ranging from 10 to 60 kGy, or the observed changes were deemed minimal (McNamara et al., 2003; Herbert et al., 2005; Radloff et al., 2008; Langley et al., 2009a; Langley et al., 2009d; Borisover et al., 2016; Skulcova et al., 2018; Wehr and Kirchhof, 2021), others reported significant changes.

Irradiation induced changes associated with the organic matter fraction of soils/sediments were reported by a number of studies including a dose-dependent (1–500 kGy) increase of CO_2 production, and changes to the polycondensation, aromaticity, and molecular weight properties of humic and fulvic acids (Da Silva et al., 1997; Goraczko and Slawinski, 2008; Goraczko et al., 2008; Kelsey et al., 2010; Zhao et al., 2020; Zhao et al., 2021). Such changes also affected the complexation affinity of the organic compounds towards Ca^{2+}, Cs^{+}, Sr^{2+}, and Eu^{3+}, as well as the sorption and bioaccumulation behaviour of the organic contaminants p,p'-DDE and anthracene (Kelsey et al., 2010; Zhao et al., 2020; Zhao et al., 2021; Zhao et al., 2022a). Dose-dependent increase of dissolved organic matter (DOM) with lower polycondensation and aromaticity was also reported by a number of studies following irradiation of soils and sediments (McNamara et al., 2003; Zhang et al., 2016). Such changes were attributed to radical-induced cleavage of C—C bonds and depolymerization of carbohydrates (Salonius et al., 1967; Lensi et al., 1991; Tuominen et al., 1994; Berns et al., 2008; Schaller et al., 2011; Buchan et al., 2012; Zhang et al., 2016; Otte et al., 2018; Buessecker et al., 2019). Accompanying the release of DOM, Schaller et al. (2011) observed a concomitant increase of dissolved Fe and Mn, and the remobilization of As and U into solution following the irradiation of organic-rich sediments to a final dose of 60 kGy. At a lower dose (20 kGy), significant reduction of Fe(III)-bearing minerals (e.g. goethite) to Fe(II) within organic poor sediment was reported by Bank et al. (2008). Consequently, this significantly modified the cation exchange capacity thereby enhancing the adsorptive capacity of the sediment towards U(VI) (Bank et al., 2008). Other reported irradiation induced changes include: (1) a 16% decrease in soil surface area (10 kGy) (Lotrario et al., 1995), (2) changes in the aggregation state of soil, resulting in an increase in surface area (36 kGy) (Berns et al., 2008), (3) slight alterations in the surface area of specific minerals and a decrease in cation exchange capacity due to the radiation-induced reduction of Fe(III) to Fe(II) within clay minerals (1.1 MGy) (Plötze et al., 2003), and (4) enhanced remobilization of uranium from sediments (30 kGy) (Seder-Colomina et al., 2022).

The contradictory findings or the extent of reported changes in the literature could be attributed to differences related to the dose applied, and the physicochemical properties of the natural sample, including mineralogy, moisture content, and organic matter content or type/stability, as well as the duration of the experiment (Salonius et al., 1967; Lotrario et al., 1995; Da Silva et al., 1997; McNamara et al., 2003; Radloff et al., 2008; Slizovskiy and Kelsey, 2010; Lees et al., 2018; Otte et al., 2018; Wehr and Kirchhof, 2021). Nonetheless, despite the fact that most studies reported an increase in DOM following γ-irradiation, few studies have examined the relationship between organic matter content and irradiation induced changes of the physicochemical properties of natural samples (Kelsey et al., 2010; Borisover et al., 2016; Skulcova et al., 2018; Buessecker et al., 2019). Moreover, given the apparent sensitivity of iron bearing minerals and organic matter to γ-irradiation, there is a significant gap in research concerning its impact on those constituents, particularly in cases where they coexist in close proximity.

Close association between organic matter and iron (oxyhydr)oxides in the environment occurs through a number of sequestration processes that remove organic matter from solution to the solid mineral particles (Kaiser et al., 1997; Kaiser, 2003; Fortin and Langley, 2005; Mikutta et al., 2008; Lalonde et al., 2012; Kleber et al., 2015; Bao et al., 2021; Curti et al., 2021; Possinger et al., 2021; Li et al., 2023). These processes include the adsorption of organic matter to the surface of preformed- and the coprecipitation of organic matter with neoformed- mineral phases where the latter comprises several interlinked complex processes (Kaiser et al., 1997; Kaiser, 2003; Schwertmann et al., 2005; Wagai and Mayer, 2007; Mikutta et al., 2008; Pedrot et al., 2011; Chen et al., 2014; Kleber et al., 2015; Curti et al., 2021; Possinger et al., 2021; Li et al., 2023). Such processes are abundant in the environment and they occur within the porewaters of soils and sediments (Wagai and Mayer, 2007; Cismasu et al., 2011; Lalonde et al., 2012; Zhao et al., 2016), oxic-anoxic transition zones where Fe(II)-bearing anoxic solutions come into contact with O_2 (Riedel et al., 2013), and industrial coagulation water treatment landfills (Henneberry et al., 2012). In addition to plant-derived organic matter, microbes also contribute to this C pool by producing polysaccharides that serve as templates for the precipitating iron (oxyhydr) oxide minerals (Chan et al., 2004; Fortin and Langley, 2005; Chan et al., 2009; Kallenbach et al., 2016; ThomasArrigo et al., 2022). These organo-mineral coprecipitates possess distinct physicochemical and mineralogical properties than minerals formed in the absence of organic matter and mineral-organic associations that form by organic matter adsorption to pre-existing mineral surfaces (Schwertmann et al., 2005; Eusterhues et al., 2008; Mikutta et al., 2008; Cismasu et al., 2011; Kleber et al., 2015; ThomasArrigo et al., 2022). Organo-mineral coprecipitates are characterized by small crystal size, defective crystallographic structure, low specific surface area, distinct aggregation state, and distinct surface charge (Eusterhues et al., 2008; Mikutta et al., 2008; Toner et al., 2009; ThomasArrigo et al., 2022). Because of these properties, organo-mineral coprecipitates have been a subject of intense research to determine their role in the environment towards contaminant, nutrient, and trace metal mobility (Grybos et al., 2007; Mikutta et al., 2014; Fabisch et al., 2016; Hao et al., 2016; Sowers et al., 2017; Chen et al., 2018; Field et al., 2019; Xue et al., 2019; Dong et al., 2022), C storage (Lalonde et al., 2012; Han et al., 2019; Patzner et al., 2022; Martens et al., 2023), long term stability (Kaiser et al., 2007; Cismasu et al., 2016; Najem et al., 2016; Zhao et al., 2022b), and susceptibility/bioavailability to microbial degradation (Langley et al., 2009b; Pedrot et al., 2011; Amstaetter et al., 2012; Shimizu et al., 2013; Eusterhues et al., 2014; Adhikari et al., 2016; Poggenburg et al., 2016; Adhikari et al., 2017; Cooper et al., 2017; Zhao et al., 2017; Mejia et al., 2018; Poggenburg et al., 2018; Han et al., 2019; Zeng et al., 2020; Dong et al., 2023). Within this context, past and ongoing research have highlighted the importance of physicochemical and mineralogical properties as well as organic matter content/type in modulating the reactivity of organo-mineral coprecipitates. Therefore, given sensitivity in reactivity of iron (oxyhydr)oxides to changes in crystallinity and organic matter content,

determining the extent of impact of γ-radiation on the reactivity of organo-mineral coprecipitates is important for future studies employing this technique to natural samples.

In this study, we examined the impact of γ-radiation on the physical and chemical properties, as well as bioavailability of various iron oxyhydroxides that were synthesized in the presence of organic matter (coprecipitation). Specifically, we synthesized 2-line ferrihydrite, lepidocrocite, and goethite - both in the presence and absence of Na-alginate. These minerals were selected for their representation of a range of thermodynamic stability, and their abundance in the environment including biogenic iron oxides (BIOS) (Cornell and Schwertmann, 2003; Fortin and Langley, 2005; Langley et al., 2009b; Gault et al., 2011; Fabisch et al., 2016; Najem et al., 2016; ThomasArrigo et al., 2022). Additionally, alginate was chosen as the organic compound due to its chemical resemblance to the twisted stalks and sheaths produced by the Fe(II)-oxidizing bacteria *Gallionella* spp. and *Leptothrix* spp., respectively, that contribute to the formation of BIOS (Chan et al., 2004; Chan et al., 2009). Polysaccharides are also important components of plant root exudates, contributing up to ~10% of the total organic matter pool in soils and sediments (Kleber et al., 2015). However, the reader should consider that alginate does not capture the response of other constituents from extracellular polymeric substances such as proteins, phosphate, and nucleic acids, as well as aromatic components from natural OM to irradiation (Tourney and Ngwenya, 2014; Kleber et al., 2015). Lastly, a total dose of 25 kGy was chosen for this study, because it represents the lower range of sterilization where most microbes in natural samples are reportedly eliminated (McNamara et al., 2003).

2. Materials and methods

2.1. Synthesis of iron oxyhydroxides and coprecipitates

Prior to mineral syntheses, all necessary glassware and components were initially submerged in 10% HNO_3 bath for a minimum duration of 24 h then washed 3× with ultrapure water (UPW) (18 MΩ•cm). The glassware was then baked in a muffle-furnace at 450 °C for a duration of 8 h to remove any residual organic matter, and then sterilized by autoclaving. Prior to use, alginate was sterilized by spreading the dry powder on the base of a beaker or Pyrex bottle followed by irradiation with an ultraviolet light source for a period of 1 h. FTIR-ATR of the UV-irradiated alginate powder revealed no discernible structural changes (data not shown). To ensure sterility, all working solutions were prepared aseptically by using sterile UPW or by filtering (0.22 μm pore size filter).

2-line ferrihydrite (Fh), lepidocrocite (Lp), and goethite (Gt) were synthesized in the absence and presence of Na-alginate at C/Fe molar ratios of 0, 0.5, 1.0, and 1.5 according to published methodologies (Glasauer et al., 2003; Mikutta et al., 2008; Schwertmann and Cornell, 2008; Langley et al., 2009b). The selected C/Fe concentrations in the coprecipitates were representative of those found in BIOS, as well as commonly occurring concentrations in soils and sediments (Chen et al., 2014; Kleber et al., 2015; Zhao et al., 2016; Field et al., 2019). A detailed description of the mineral synthesis procedures is given in the Supplementary Material. Briefly, Fh was synthesized from the neutralization of a ferric chloride solution with a base (1 M NaOH) to pH ~7.00 (Glasauer et al., 2003; Langley et al., 2009b) consistent with studies researching synthetic Fh-OM-coprecipitates (Shimizu et al., 2013; Adhikari et al., 2016; Adhikari et al., 2017). Lp was synthesized from the oxidation of a ferrous chloride solution while manually maintaining the pH at 6.7–6.9 with a base (1 M NaOH) (Schwertmann and Cornell, 2008). This chosen method precludes the addition of contaminating additives and high temperature (e.g. 50 °C or 70 °C) (Schwertmann and Cornell, 2008), which may damage the structure of alginate. High surface area Gts representative of those occurring in BIOS were synthesized at pH 7 from the oxidation of a ferrous chloride solution in the presence of bicarbonate (HCO_3^-:Fe ~2) (Schwertmann and Cornell, 2008; Gault et al., 2011). For each mineral, washing of the precipitates proceeded by centrifugation/vortexing and washing with sterile UPW until the conductivity of the supernatant decreased to <25 μS/cm. Subsequently, for each mineral, the precipitates were equally divided and aseptically combined into 2 separate straight sided glass jars (60 mL) with polypropylene screw caps, thoroughly homogenized in open atmosphere, and stored for a maximum period of 10 days at 4 °C until the radiation treatment. It should be noted that the wet precipitates occupied ~90% of the jar volume, and sterile UPW was added where deemed necessary to reduce the volume of the headspace. The final total Fe concentration for each mineral in the jars are given in Table S1.

2.2. Gamma (γ)-irradiation

For each mineral synthesized, one of the two jars was placed in a 2 L glass beaker and transported on ice to Nordion (Canada) Inc. where γ-irradiation proceeded using a ^{60}Co source at a rate of 12–15 kGy/h to a total dose of ~25 kGy. Prior to irradiation, ice cubes were added to the beaker and distributed in between and on top of the jars to mitigate any temperature increase during the irradiation treatment. Ice was added again at the mid-point of the irradiation process at which point the ice was observed to have melted. Upon completion of the treatment, the samples were transported back to the laboratory on ice and then quickly stored in the fridge at 4 °C until use. Shipping, treatment, and handling of the samples were carried out within 3 h.

2.3. Characterization of the iron oxyhydroxides

For a particular mineral, both the non- and its γ-irradiated counterpart were subsampled in tandem to avoid any variability in reactivity due to ageing and/or handling. Initially, the jars were centrifuged at 4200 rpm for 10 min and, where possible, the supernatant was aseptically transferred in its entirety into a 40 mL VOA glass vial which was then immediately transferred into an anoxic chamber for subsequent analyses (*Section 2.4*). The separated iron oxyhydroxide precipitates were aseptically homogenized, and then characterized for their physicochemical properties (*Sections 2.3.1–2.3.5*) and bioavailability (*Section 2.5*) as described below.

2.3.1. ^{57}Fe Mössbauer spectroscopy

Given the sensitivity of ferrihydrite to structural alteration, only the native and post-irradiated 2-line ferrihydrite samples were analysed with ^{57}Fe Mössbauer spectroscopy. Samples for analyses were handled and dried under an anoxic atmosphere composed of a mixture of 95% N_2 and 5% H_2. The powdered samples were loaded into Plexiglas holders (area: 1 cm^2), forming a disc. These samples were kept in airtight jars at −20 °C until measurement. Holders were inserted into a closed-cycle exchange gas cryostat (Janis cryogenics, USA) under a backflow of He to minimize exposure to air. Spectra were collected at 77 K and 5 K using a constant acceleration drive system (WissEL, Germany) in transmission mode with a ^{57}Co/Rh source. All spectra were calibrated against a 7 μm thick α-^{57}Fe foil that was measured at room temperature. Analysis was carried out using Recoil (University of Ottawa) and the extended Voigt Based Fitting (VBF) routine (Lagarec and Rancourt, 1997). The half width at half maximum (HWHM) was constrained to 0.123 mm/s during fitting.

2.3.2. Powder X-ray diffraction, specific surface area, and Fourier transform infrared spectroscopy

The bulk mineralogy of the native and γ-irradiated iron oxyhydroxides was determined by X-ray diffraction (XRD). Air-dried samples were thoroughly ground to fine powders with an agate mortar and pestle and analysed with a Rigaku Ultima IV diffractometer using a Cu-Kα X-ray source, operating at 45 kV and 40 mA. Continuous scans were run from 10 to 80° 2Θ using a step size of 0.02° at a rate of 0.7°/min. Specific surface area (SSA) measurements on duplicate samples

prepared in the same manner as XRD were carried out using a Quantachrome Autosorb-1. Approximately, 100–300 mg of a sample was initially degassed under vacuum at 50 °C for 24 h using a 9 mm cell. After the determination of degassing stability and final dry mass, 33 N_2 adsorption and 19 desorption points were recorded at 77 K in the partial pressure region 5×10^{-3}- 0.99 P/P_0. The SSA was determined by applying the BET equation on the standard partial pressure region (0.05–0.3 P/P_0) or by applying the criteria established by Rouquerol et al. (2007) where deemed necessary. The micropore volume was determined by applying the Dubinin-Radushkevich (DR) method to adsorption points below 0.01 P/P_0, whereas the mesopore volume (2–50 nm) was determined by applying the Barrett-Joyner-Halenda (BJH) method as determined by the accompanying Autosorb-1 software (Mikutta et al., 2008; Poggenburg et al., 2016). Total pore volume was determined from the last point of the N_2 adsorption isotherm (0.99 P/P_0). Lastly, the mineral SSA and pore volumes were corrected for the weight of retained alginate content as described in Mikutta et al. (2008).

Powdered samples were also analysed with Fourier Transform Infrared Spectroscopy (FTIR) using a Nicolet 6700 spectrophotometer (ThermoFisher Scientific) equipped with a deuterated triglycine sulfate (DTGS) detector and a diamond crystal coated with ZnSe in attenuated total reflectance (ATR) mode. Prior to analyses, the powdered samples were dried under vacuum in an Oxoid™ Anoxic jar (~27 inHg below atmosphere) at 50 °C for a period of 24 h to minimize the contribution of surface adsorbed H_2O to the spectra. While at 50 °C, the samples were flushed with pure nitrogen (GR 4.5) and allowed to cool in a desiccator until analyses. Four individual measurements were made on duplicated samples (2 measurements each) in order to determine the homogeneity of sample in terms of particle size and composition together with instrumental reproducibility. For each sample, spectra were acquired from 4000 to 500 cm^{-1} at 4 cm^{-1} resolution, with 128 scans averaged per spectrum. Subsequently, the spectra were processed using the OMNIC software package (Thermo Fisher Scientific, version 9) where the spectra were averaged, automatically baseline corrected, and normalized to the maximum absorbance value.

2.3.3. Iron and carbon content

The pseudo-total iron content of dry powdered or wet samples was determined by suspending a known amount into 6 mL of UPW, and fully digested by the addition of 4 mL trace metal grade 30% H_2O_2 and 2 mL trace metal grade HNO_3 followed by heating at 75 °C for 24 h. After dilution with 1% HNO_3 (*v*/v), the Fe content was determined via inductively coupled plasma — optical emission spectroscopy using a Varian Vista-PRO CCD Simultaneous ICP-OES, operating under standard conditions. All digestions were carried out in duplicates (powdered samples) or triplicates (wet samples). For carbon content determination, approximately 10 mg of a dry powdered sample was weighed into a tin capsule. The prepared samples were then analysed for carbon content at the University of Ottawa at the Jan Veizer Stable Isotope Laboratory using the Elementar Vario Isotope Cube.

2.3.4. Chemical extractions

To determine the poorly-crystalline Fe fraction in the non- and γ-irradiated precipitates, chemical extractions were carried out in triplicates following a the methods outlined in Kostka and Luther (1994) with some modifications. Briefly, ~20 mg of wet sample was accurately weighed into 20 mL scintillation vials followed by the addition of either HCl (0.5 M) or ascorbate (pH 8.0). The HCl extraction proceeded under oxic conditions for a duration of 1 h, whereas the ascorbate extraction proceeded under anoxic conditions for a duration of 24 h in the dark. Following extraction with HCl (0.5 M), the digests were filtered (Cytiva polyethersulfone membrane, 0.22 μm) and an aliquot was analysed with the ferrozine assay to determine the Fe(II) content ($HCl_{Fe(II)}$), and another aliquot was reduced with 0.28 M ClH_4NO in 0.28 M HCl for a duration of 30 min to determine total Fe ($HCl_{totalFe}$) concentration following determination with the ferrozine assay (Stookey, 1970; Kostka and Luther, 1994; Viollier et al., 2000). The 0.5 M HCl extractable Fe(III) was calculated as $HCl_{Fe(III)} = HCl_{totalFe} - HCl_{Fe(II)}$. For the ascorbate extraction, the digests were filtered (Cytiva polyethersulfone membrane, 0.22 μm) under anoxic conditions and the filtrates were analysed using the ferrozine assay. To determine the fraction of amorphous Fe in the precipitates, the concentration of Fe extracted by ascorbate or HCl was normalized by the total Fe concentration (*Section 2.3.3.*).

2.3.5. Electrophoretic mobility and particle size

The electrophoretic mobility (EM) and particle size of the iron oxyhydroxides was measured in a filtered (Sartorius polyethersulfone membrane, 0.22 μm) 10 mM $NaNO_3$ solution using a Zetasizer Nano-ZS (Malvern, Instruments) at 25 °C. Initially, the iron oxyhydroxides were dispersed by adding a wet sample (equivalent to 25–30 mg of dry solid per litre) to 500 mL of background electrolyte and stirred for 1 h. Subsequently, the pH of 50 mL aliquots was adjusted with filtered 10 mM NaOH or HNO_3 to a constant desired value between pH 3–9. The EM measurements were determined from the average of 5 runs comprising of 10 cycles each. Particle size of the suspensions was determined from the average of two individual measurements taken at pH ~6 in automatic mode.

2.4. Characterization of the supernatants

The liquid portions that remained after the separation of solids from the suspensions via centrifugation, i.e. supernatants, were vacuum filtered (Sartorius polyethersulfone membrane, 0.22 μm) into 40 mL glass VOA vials under anoxic conditions. Prior to filtering, the filter membrane was rinsed by passing 500 mL of anoxic deionized water through followed by a few mL of a sample which were discarded. Subsequently, a 0.5 mL aliquot of a filtrate was preserved in 4.5 mL of 0.5 M trace metal grade HCl in the dark until analysis for dissolved Fe(II) using the ferrozine assay. For the determination of total dissolved Fe, 0.5 mL of a filtrate was digested in duplicates and analysed as described above (*Section 2.3.3.*). For the determination of the dissolved carbon content, where possible, a known volume of a filtrate was diluted into UPW and analysed at the University of Ottawa using a modified OI Analytical model 1030 wet TOC analyser. No precipitation of separate iron oxyhydroxides phases was observed following dilution. Finally, where possible, aliquots of the filtrates were also dried at 40 °C for characterization with FTIR-ATR as described above (*Section 2.3.2.*).

2.5. Bioavailability

The sterility of the native and γ-irradiated precipitates was initially confirmed by aseptically suspending sub-samples of a precipitate into 5 mL of tryptic soy broth (TSB) and allowed to incubate for 1 week. Sterility of all precipitates was confirmed by the lack of development of turbidity.

2.5.1. Microbial medium and preparation of cultures

Microbial Fe(III) reduction experiments were carried out with a well characterized, facultative, dissimilarity Fe(III)-reducing bacterium, *Shewanella putrefaciens* strain CN32 (*S. putrefaciens* CN32). Microcosm reduction experiments were carried out in a chemically defined medium (CDM) (pH ~6.7) composed of 20 mM sodium lactate as the electron donor, 4 mM 1,4-piperazinediethanesulfonic acid (PIPES) buffer, mineral salts solution, and trace metals solution (Glasauer et al., 2003; Langley et al., 2009a). For transfer into CDM, *S. putrefaciens* CN32 was initially revived from a glycerol stock solution by streaking onto tryptic soy agar (TSA) plates at room temperature (~22 °C). For inoculation, the bacteria were prepared according to the protocols of Glasauer et al. (2003) and Langley et al. (2009). Briefly, cells were prepared by aseptically inoculating 50 mL of TSB with a colony of *S. putrefaciens* CN32 from TSA plates, and kept on a stir plate (125 rpm) for 24 h at 22 °C. Subsequently, 0.5 mL of the culture was transferred into 50 mL of 50:50

CDM:TSB mixtures. After 24 h, the passaging procedure was repeated with 95:5 CDM:TSB containing 100 μM phosphate, and continued by transferring into 99:1 CDM:TSB containing 200 μM phosphate for a period of 30 h. The final step involved growing the bacteria in 100% CDM containing 400 μM phosphate for a period of 36 h. The concentration of phosphate was progressively increased to acclimate the bacteria to depleted nutrients and microcosm conditions (Glasauer et al., 2003; Langley et al., 2009b). Following the acclimation period, the bacteria were harvested by centrifugation at 4000 rpm and the cell pellet was re-suspended into 2 mL of fresh, sterile CDM. Finally, the BioRad Protein Assay II dye reagent was used to standardize the concentrated cell suspension in order for the microcosms to contain a cell density of $\sim 10^7$ CFU/mL (Glasauer et al., 2003; Langley et al., 2009b).

The experimental setup consisted of 500 mL acid-washed Pyrex bottles (microcosms) containing 450 mL of sterile CDM amended with 4 mM Fe in the form of iron oxyhydroxide, and 400 μM of sodium phosphate. The experiments were conducted in triplicates and controls to which no bacteria were added were included. Prior to inoculation with *S. putrefaciens* CN32, the microcosms were wrapped in aluminium foil in order to avoid potential photochemical reactions and then transferred into an anoxic chamber where inoculation proceeded. Throughout the paper, we refer to the microcosms to which cells were added as "biotic" microcosms, whereas controls to which no bacteria were added are referred to as "control" microcosms. It should be noted that for a mineral phase, the microcosms for the native precipitate and its γ-irradiated counterpart were set up and inoculated in tandem to minimize potential variations due to media preparation (pH, temperature) and culture preparation (inoculum size and the state of the cells) (Glasauer et al., 2003).

2.5.2. Sampling and analyses

Sampling of each system was performed immediately following the addition of the cells (time 0) and then periodically at selected time points. Sampling was carried out by vigorously shaking the microcosms to suspend the iron oxides into solution. Immediately, 20 mL of the suspension was poured into a sterile 20 mL scintillation vial from which all sub-sampling proceeded to minimize the potential contamination of the microcosms (Langley et al., 2009a). The sub-sampled suspensions were analysed for pH, cell viability (at the start and end of the experiment), total and dissolved Fe(II), and total Fe. pH was monitored utilizing standard calibrated laboratory meters and probes, whereas cell viability was determined by colony counts on TSA plates (Glasauer et al., 2003; Langley et al., 2009a). Fe(II) associated with the solid phase (total Fe(II)) was determined by dispensing 1 mL of unfiltered iron oxyhydroxide suspension into 1 mL of trace metal grade 6 M HCl (final concentration of 3 M) and allowed to digest for at least 24 h under anoxic conditions prior to dilution and analysis via the ferrozine assay (Stookey, 1970; Viollier et al., 2000). Dissolved Fe(II) was determined by filtering (0.22 μm) 6 mL of the suspension into an acid-washed 20 mL scintillation vial, and immediately dispensing 0.5 mL of the filtrate into 4.5 mL of trace metal grade 0.5 M HCl. Digestion proceeded for at least 24 h under anoxic conditions prior to analysis by the ferrozine assay. To determine total Fe, 2 mL of the unfiltered iron oxyhydroxide suspensions were digested with 2 mL of trace metal grade 12 M HCl for a period of 24 h. Following dilution, Fe determination proceeded by dispensing 100 μL aliquot of the digest into 900 μL of 0.28 M ClH_4NO in 0.28 M HCl for a duration of 30 min and then determining the concentration of Fe^{2+} using the ferrozine assay.

2.5.3. Biogenic solids

At the end of the experimental period, post-reduction minerals were collected by centrifugation (3000 rpm), washed 3× with anoxic UPW, and dried under anoxic conditions. The powdered precipitates were analysed by XRD as described above, using an air sensitive sample holder in order to prevent the oxidation of potential Fe(II)-bearing minerals.

3. Results

3.1. Chemistry of supernatants

Irradiation induced physical changes to the coprecipitates were visually apparent with changes being most obvious for the ferrihydrite (Fh) coprecipitates (C/Fe 0.5, 1.00, and 1.5) (Fig. S1). Prior to irradiation, the Fh coprecipitates exhibited a viscous gel-like texture which upon irradiation, 40–80% of their volume was converted into a brown liquid (Fig. S1). The pH of the supernatants collected from the various iron oxyhydroxides remained more-or-less neutral and did not exhibit a substantial change following irradiation nor did it exhibit a specific trend (Fig. S2). However, in some cases the pH of the supernatants slightly decreased following irradiation, which was attributed to the oxidation of ferrous iron and subsequent hydrolysis of ferric iron (Fig. S2). Fig. 1 shows the amount of dissolved Fe species (Fe(II) and total Fe (Fe(II) + Fe(III)) and organic carbon (DOC) in the filtered supernatants relative to the initial total concentration (Table S1). The amount of dissolved Fe species in the supernatants of the pure iron oxyhydroxides was low and did not change post-irradiation (Fig. 1). For the native Fh coprecipitates, a liquid sample could only be collected from Fh coprecipitated with C/Fe of 0.5 and it did not contain a measurable amount of dissolved Fe species or DOC (Fig. 1). However, following irradiation of the Fh coprecipitates, the amount of dissolved Fe species and DOC increased linearly with increasing initial C/Fe ratio (Fig. 1). The relative amount of the dissolved Fe(II) and total Fe were within the range of 0.1–0.7%, and 3.5–9%, respectively (Fig. 1). This increase was accompanied by an increase in DOC falling within the range of 2–35% (Fig. 1).

Dissolved Fe species were also detected in the supernatants of the native lepidocrocite (Lp) and goethite (Gt) coprecipitates, a probable consequence of the incomplete oxidation of Fe(II) and complexation of Fe/stabilization of Fe-colloids by alginate which remained in suspension (Fig. 1). Such notion is supported by the detection of DOC in the supernatants of these systems (Fig. 1). As was observed for the Fh coprecipitates, irradiation led to significant difference in the amount of dissolved Fe(II), total Fe, and DOC in the supernatant of these systems when compared to their native controls ($P < 0.05$) (Fig. 1). Following irradiation of the Lp coprecipitates, the amount of dissolved Fe(II), total Fe, and DOC increased by 9-15×, 16-23×, and 2.5-3×, respectively, relative to native controls (Fig. 1). Similarly, for the irradiated Gt coprecipitates, the amount of dissolved Fe(II), total Fe, and DOC increased by 40-100×, 30-50×, and 1.1–2×, respectively, relative to the native controls (Fig. 1). For the irradiated Lp and Gt coprecipitates, apart from Gt with C/Fe of 1.5, it was also observed the amount of the dissolved Fe species as well as DOC increased with increasing initial concentration of alginate (Fig. 1). Across all the irradiated coprecipitates, dissolved Fe(II) made up a small proportion of the total dissolved Fe pool indicating that the majority of this pool was comprised of oxidized Fe (III) species (Fig. 1).

3.2. Chemistry of solids

Fig. 2 shows the total, ascorbate and 0.5 M HCl extractable Fe content of the native and irradiated iron oxyhydroxides normalized by their wet mass. Also shown is the proportion of 0.5 M HCl extractable Fe(II), as well as the C/Fe molar ratio measured in the dry native and post-irradiated iron oxyhydroxides (Fig. 2). Post-irradiation, the total Fe content was found to increase especially for the coprecipitates (Fig. 2). The amount of Fe extracted from the post-irradiated Fh precipitates by either extractant was either equivalent to the total Fe (100% extraction) or did not significantly differ ($P > 0.05$, two tailed *t*-test) from that of the native controls (Fig. 2). Also, as was observed with pure Fh, irradiation did not significantly affect the 0.5 M HCl nor the ascorbate extractable Fe fraction of the pure Lp and Gt ($P > 0.05$, two tailed t-test, Fig. 2). Conversely, post-irradiation, the 0.5 M HCl extractable Fe fraction from

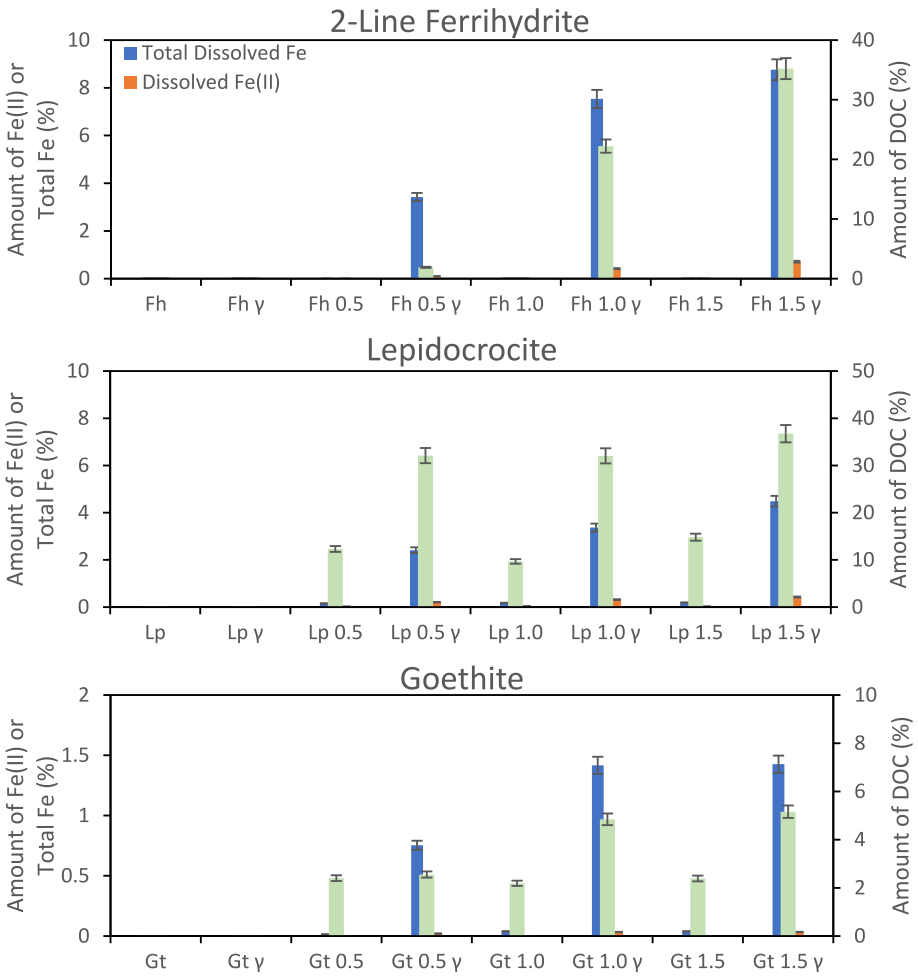

Fig. 1. Amount of dissolved Fe(II), total Fe, and organic carbon (DOC) measured in the filtered (0.22 μm) aqueous supernatants collected following the centrifugation of the native iron oxyhydroxides and their corresponding γ-irradiated counterparts. The amounts are reported relative to the total initial amount in the jars. The data represents the mean ± standard deviation of two measurements from each supernatant collected. Note the scale for the goethite precipitates.

the Lp coprecipitates significantly decreased by 30–40%, but it did not exhibit a specific trend ($P < 0.05$, two tailed t-test, Fig. 2). However, ascorbate extractable Fe did not significantly differ between the corresponding native and irradiated Lp coprecipitates ($P > 0.05$, two tailed t-test, Fig. 2). Interestingly, irradiation of Gt coprecipitated with C/Fe ratio of 0.5 significantly decreased the 0.5 M HCl and ascorbate extractable Fe by ~20% ($P < 0.05$, two tailed t-test, Fig. 2). In contrast, for Gt coprecipitates with C/Fe ratio of 1.0 or 1.5, both extractants recovered comparable amounts of Fe ($P > 0.05$, two tailed *t*-test, Fig. 2). The fraction of Fe(II) associated with the solid phase (adsorbed/structural) was expected to increase following irradiation, as was observed in the supernatants of the coprecipitates (Fig. 2). However, among the iron oxyhydroxide studied, 0.5 M HCl extractable Fe(II) did not increase following irradiation nor did it show a specific trend, and this can be attributed to the possible oxidation of Fe(II) during mixing/weighing of the iron oxyhydroxides in open atmosphere (Fig. 2).

Irradiation induced changes to the C/Fe content of the coprecipitates were also investigated (Fig. 2). A minor amount of C was measured in the pure iron oxyhydroxides which likely originated from the adsorption of atmospheric carbonate (Fh and Lp) or from the addition of bicarbonate (Gt) during synthesis (Fig. 2). Post-irradiation, no change was observed in the C/Fe ratio for the pure phases whereas the C/Fe ratio was observed to decrease for specific coprecipitates (Fig. 2). For instance, the C/Fe remained the same for Fh with C/Fe ratio of 0.5, but significantly decreased by ~10 and 30% for Fh coprecipitated with C/Fe ratios of 1.0 and 1.5, respectively. Such changes appeared to increase with increasing initial alginate content ($P < 0.05$, two tailed *t*-test, Fig. 2). For the Lp coprecipitates with C/Fe ratios of 0.5 and 1.5, the C content significantly decreased by 12 and 9%, respectively, post-irradiation ($P < 0.05$, two tailed t-test, Fig. 2). Although the C content also decreased for the post-irradiated Lp coprecipitated with C/Fe 1.0 such decrease was not significant ($P > 0.05$, two tailed t-test, Fig. 2). Finally, irradiation did not significantly affect the C content of the Gt coprecipitates ($P > 0.05$, two tailed t-test, Fig. 2).

3.3. Specific surface area and porosity

The N_2 adsorption-desorption isotherms for the various studied iron oxyhydroxides are presented in Figs. S3-S5, whereas Fig. 3 summarizes the derived specific surface area (SSA) and pore volumes, including micropore (MIV), mesopore (MEV), and total pore (TPV) volumes. The N_2 adsorption-desorption isotherm shapes of the post-irradiated iron oxyhydroxides closely resembled their corresponding native controls (Figs. S3-S5). However, a distinction was observed with the post-irradiated Fh coprecipitates, specifically those with C/Fe ratios of 0.5 and 1.0, which exhibited reduced N_2 adsorption compared to their native controls (Figs. S3). It was found that irradiation had a significant impact on the porosity and SSA of Fh coprecipitates with C/Fe ratios of 0.5 or 1.0 ($P < 0.05$, two tailed t-test. Fig. 3). After irradiation, the MIV, TPV, and SSA of Fh coprecipitated with C/Fe of 0.5 decreased by approximately 15%, 20%, and 15%, respectively, while MEV remained unchanged (Fig. 3). Similarly, the post-irradiated Fh coprecipitated with

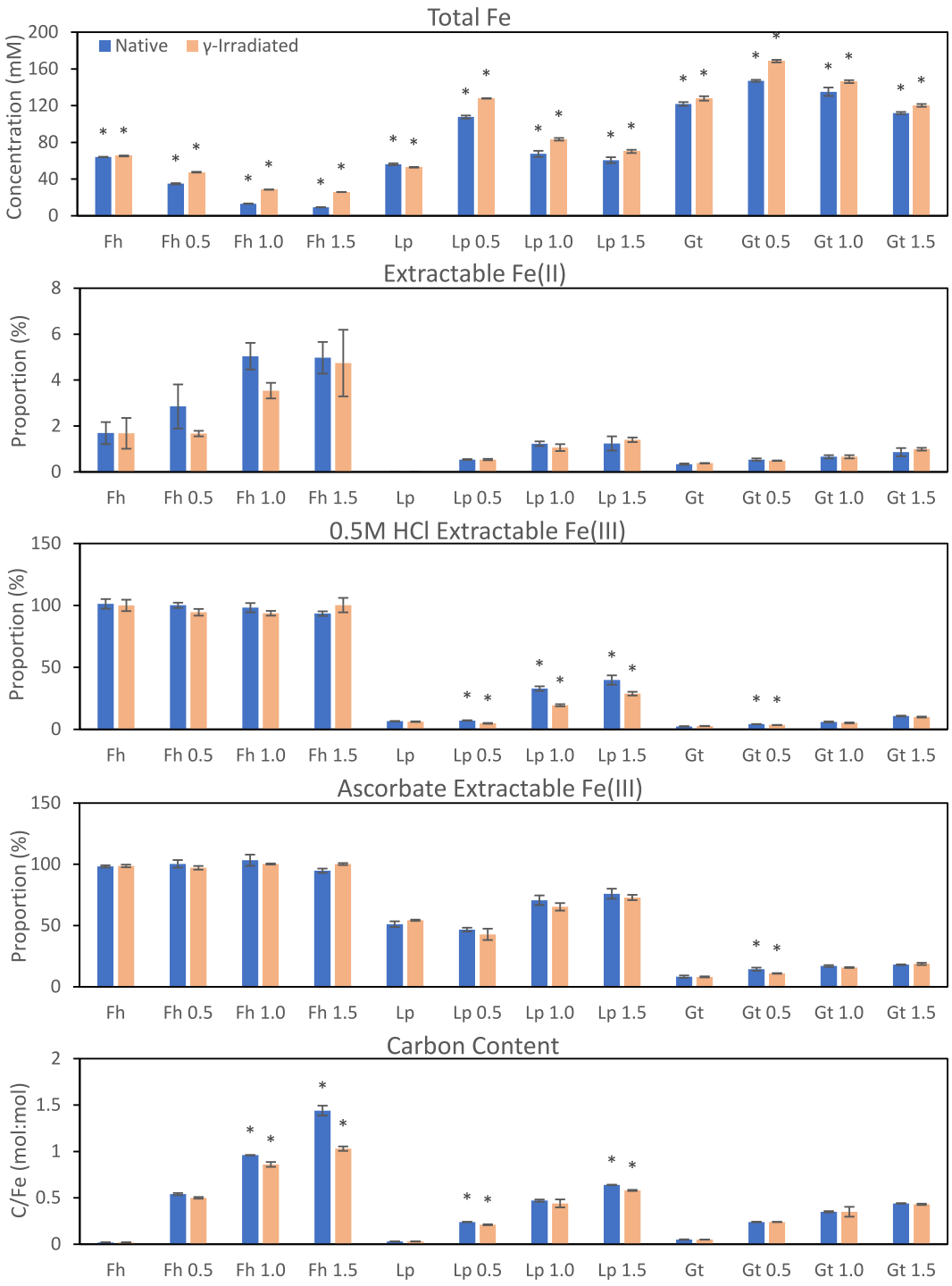

Fig. 2. Chemical extractions of the solid iron phase of the native iron oxyhydroxides and their corresponding γ-irradiated counterparts. The fractions of poorly crystalline Fe containing phases as determined by 0.5 M HCl and ascorbate are presented relative to the total Fe. The figure includes the C/Fe molar ratios determined from the solid native and γ-irradiated precipitates. Values for the chemical extractions correspond to the mean ± standard deviation of three replicates, whereas values for the C/Fe molar ratios correspond to the mean ± standard deviation of two replicates. Fh, Lp, and Gt correspond to 2-line ferrihydrite, lepidocrocite, and goethite, respectively.

C/Fe of 1.0 exhibited a decrease of around 40% in MIV, 40% in MEV, 50% in TPV, and 45% in SSA (Fig. 3). It was also found that despite having a similar C/Fe content, the SSA of irradiated Fh coprecipitated with C/Fe of 1.5 remained significantly lower than that of native Fh coprecipitated with C/Fe of 1.0 (Figs. 2 and 3). Finally, for all other iron oxyhydroxides studied, there were no significant changes in MIV, MEV, TPV, or SSA post-irradiation in comparison to their native counterparts ($P > 0.05$, two tailed t-test, Fig. 3).

3.4. Surface charge and particle size

Plots of the ζ-potential versus pH for the native and post-irradiated minerals are presented in Figs. S6-S8. Native coprecipitates exhibited a reduced pH_{iep} when compared to that of their corresponding pure mineral phases, in agreement with past studies (Mikutta et al., 2008). The pH_{iep} of the native pure minerals Fh, Lp, and Gt were estimated to be 7.2, 7.4, and 7.6, respectively, which were comparable to those

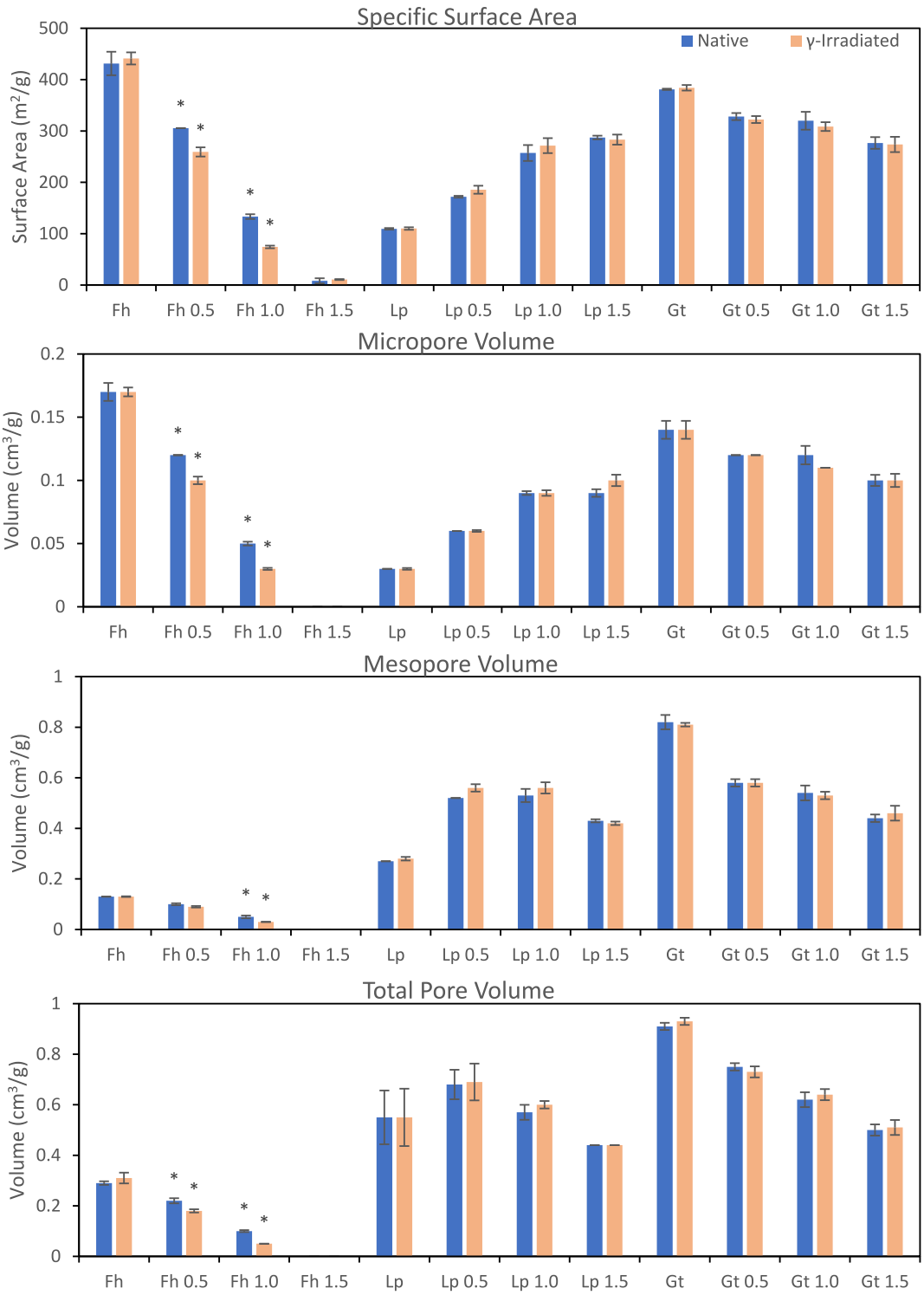

Fig. 3. Specific surface area, micropore volume, mesopore volume, and total pore volume values of the native iron oxyhydroxides and their corresponding γ-irradiated counterparts. Data points represent the mean ± standard deviation of two replicates. Data extracted from the N_2 adsorption-desorption isotherms provided in Fig. S3-S5. Fh, Lp, and Gt correspond to 2-line ferrihydrite, lepidocrocite, and goethite, respectively. Asterix indicates significance in difference between values at the 95% confidence interval ($P < 0.05$, two tailed t-test).

determined for their corresponding irradiated counterpart (Figs. S6-S8). Irradiation of the Fh coprecipitates led to some changes in their surface charge when compared to that of their native corresponding counterparts. Namely, for the Fh coprecipitate with a C/Fe ratio of 0.5, the pH_{iep} decreased from ~6.6 to ~3.6 post-irradiation (Fig. S6). The opposite was observed for the Fh coprecipitates with C/Fe ratio of 1.0 and 1.5, whereby their surface charge became more positive post-irradiation (Fig. S6). In contrast, post-irradiation, the surface charge of the Lp and Gt coprecipitates remained comparable to that of their native counterparts (Figs. S7 and S8).

Fig. 4 shows the particle size measurements of the native and post-irradiated minerals. For the native Fh minerals, the particle size generally increased with increasing alginate content, although the particle size of the coprecipitates exhibited significant variability as seen from

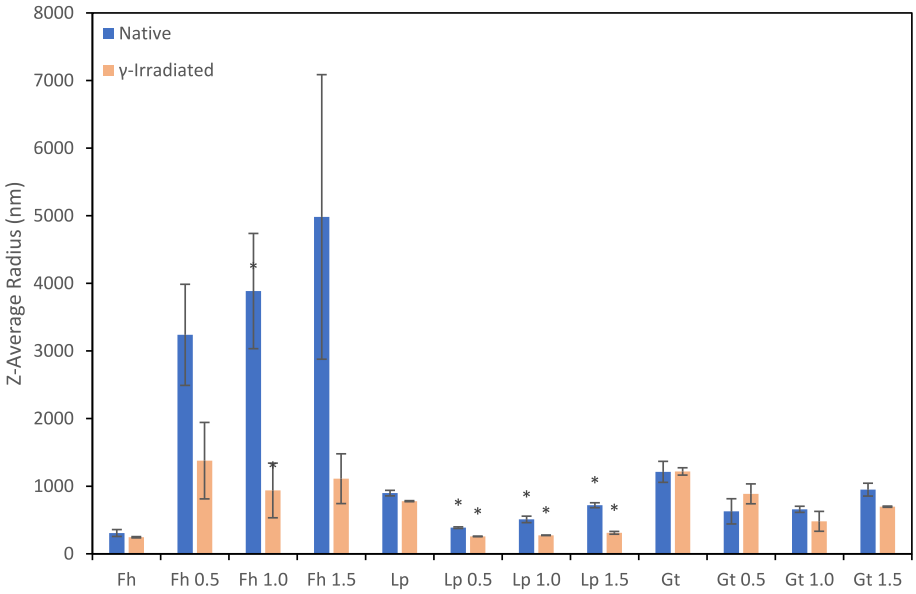

Fig. 4. Size of particles (*Z*-average) measured native iron oxyhydroxides and their corresponding γ-irradiated counterparts. Data represents the mean ± standard deviation of 2 individual replicates. Asterix indicates significance in difference between values at the 95% confidence interval ($P < 0.05$, two tailed t-test). Fh, Lp, and Gt correspond to 2-line ferrihydrite, lepidocrocite, and goethite, respectively.

the large error bars indicative of variable particle size distribution (Fig. 4). Following irradiation, the particle size of the pure Fh did not change, whereas for the Fh coprecipitates it substantially decreased suggesting changes in the particle size distribution (Fig. 4). However, significant difference in the average particle size was only observed between native and post-irradiated Fh coprecipitated with C/Fe ratio of 1.0 ($P < 0.05$, two tailed t-test, Fig. 4).

For the native Lp minerals, the particle size decreased as the alginate content increased to C/Fe ratio of 0.5, which increased with increasing alginate content (Fig. 4). Post-irradiation, similar changes were observed for the Lp minerals as in Fh minerals; however, across all of the Lp coprecipitates analysed, there was a significant decrease in particle size ($P < 0.05$, two tailed t-test, Fig. 4). The particle size of the native Gt minerals also decreased as the alginate content increased to C/Fe ratio of 0.5. This size remained constant as the initial C/Fe ratio increased to 1.0 but increased as the initial alginate content increased to C/Fe ratio of 1.5 (Fig. 4). However, unlike Fh and Lp coprecipitates, the particle size of post-irradiated Gt coprecipitates did not show significant changes and remained relatively constant ($P > 0.05$, two tailed t-test, Fig. 4).

3.5. Mineralogy

3.5.1. X-ray diffraction

Fig. 5 shows the x-ray diffraction patterns of the different iron oxyhydroxide phases before and after γ-irradiation. Reflections indicative of 2-line ferrihydrite, lepidocrocite, and goethite were identified in the diffractograms, and they corresponded closely with those published in the literature (Schwertmann and Cornell, 2008). Substantial differences between the diffractograms of a native and its corresponding γ-irradiated counterpart were not evident, suggesting that, at the bulk level, γ-irradiation did not affect the mineralogy of the studied minerals (Fig. 5). Additionally, a comparison of the full width at half maximum (FWHM) between native minerals and their γ-irradiated counterparts showed no substantial differences (data not shown).

3.5.2. Fourier transform infrared spectroscopy

Additional information about the chemical composition, functional groups, and degree of crystallinity was obtained through FTIR spectroscopy. The IR spectrum for Na-alginate is presented in Fig. S9, and the corresponding band assignments are given in Table S2. The IR spectra within the 1800–800 cm^{-1} region of the native and post-irradiated Fhs are presented in Fig. 6. The complete IR spectra of the studied iron oxyhydroxides are presented in Figs. S10-S12, and the assignments of the most characteristic vibrational modes are summarized in Tables S3-S5 as determined by theory and the literature (Sartori et al., 1997; Chandıa et al., 2001; Cornell and Schwertmann, 2003; Leal et al., 2008; Schwertmann and Cornell, 2008; Cardenas-Jiron et al., 2011).

The spectra of γ-irradiated Fh coprecipitates exhibited most of the characteristic absorption bands of their native counterparts with a slight shift in wavenumbers but displayed some notable differences (Figs. 6 and S10). Among all of the post-irradiated Fh coprecipitates, the centre of the broad stretching O—H band ν(O—H) shifted to higher wavenumbers (Fig. S10). Specifically, this band shifted from 3205 cm^{-1}, 3206 cm^{-1}, and 3177 cm^{-1} to 3215 cm^{-1}, 3216 cm^{-1}, and 3204 cm^{-1} post-irradiation for Fh coprecipitates with C/Fe ratios of 0.5, 1.0, and 1.5, respectively (Fig. S10). Additionally, post-irradiation, the intensity of this band decreased for Fh coprecipitates with C/Fe of 0.5 and 1.0 but remained.

unchanged for Fh coprecipitated with C/Fe of 1.5 (Fig. S10). The observed shifting and changes in intensity of this band suggests possible changes related to strength of the hydrogen bonds or water uptake. Changes to the intensity of the bands corresponding to alginate were also evident (as determined by measurement of peak heights), consistent with the decrease of C content, post-irradiation (Figs. 3 and 6, and Fig. S10). Specifically, for Fh with a C/Fe ratio of 0.5, the intensity of the carboxylate asymmetric stretching band (ν_{asym}(C-O-O), 1590–1592 cm^{-1}) increased by ~16%, the symmetric stretching band (ν_{sym}(C-O-O), 1406–1408 cm^{-1}) remained unchanged, while the asymmetric stretching of the glycosidic linkage band (ν_{asym}(C-O-C) ~1024–1030 cm^{-1}) decreased by ~20% post-irradiation (Fig. 6). For Fh with a C/Fe ratio of 1.0, the intensity of the carboxylate asymmetric stretching band remained the same, the symmetric stretching band decreased by ~11%, and the asymmetric stretching of the glycosidic linkage band decreased by ~17% post-irradiation (Fig. 6). For Fh with a C/Fe ratio of 1.5, the intensity of the carboxylate asymmetric stretching band remained the same, the symmetric stretching band decreased by ~16%, and the asymmetric stretching of the glycosidic linkage band decreased by ~21% post-irradiation (Fig. 6). Across all post-irradiated Fh coprecipitates, it was also observed that the band corresponding to the asymmetric stretching of the carboxylate groups broadened due to the

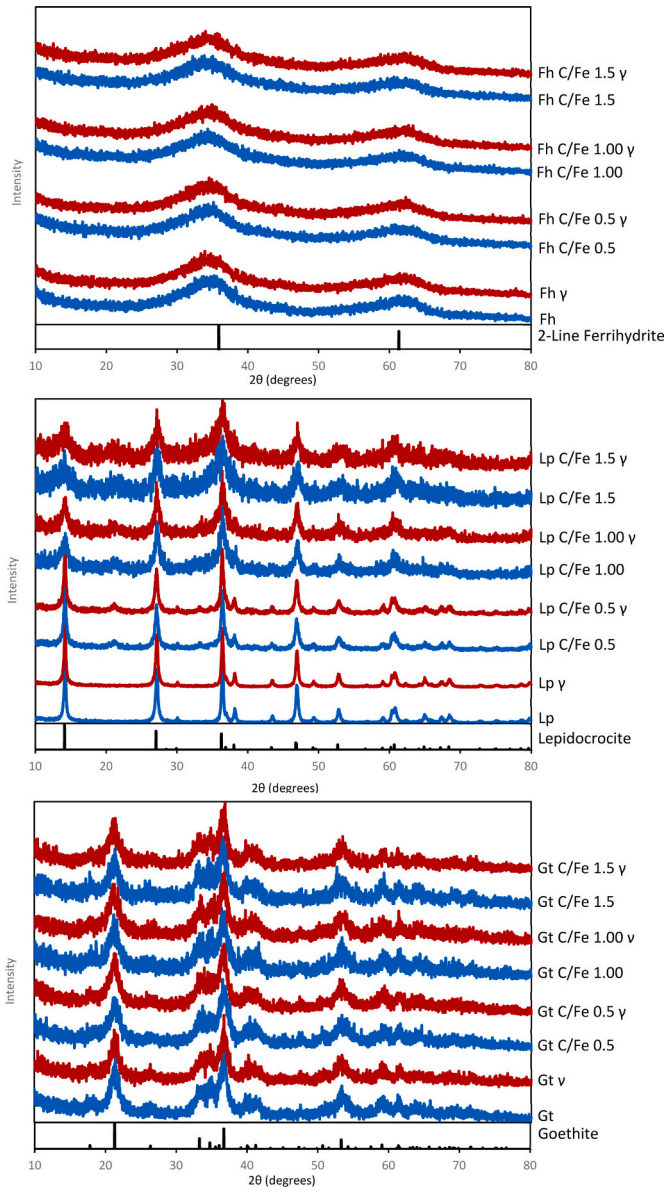

Fig. 5. Powder x-ray diffractograms of the native iron oxyhydroxides and their corresponding γ-irradiated counterparts compared to the standard reference lines. For clarity, all patterns have been vertically separated on an arbitrary y-axis. Fh, Lp, and Gt correspond to 2-line ferrihydrite, lepidocrocite, and goethite, respectively.

possible appearance of a shoulder band (Fig. 6).

Irradiation did not influence the mineralogy of pure Lp as the bands position and intensity were similar to those of the native Lp (Fig. S11). Similarly, the IR spectra of the post-irradiated Lp coprecipitates also exhibited most of the characteristic absorption bands of their corresponding native counterparts, suggesting minimal irradiation induced changes in crystallinity and mineralogy (Fig. S11). Across all post-irradiated coprecipitates, the intensity of the band centered at ~1022 cm^{-1} corresponding to the in-plane δ(O—H) vibration of the Lp mineral decreased (Fig. S11). However, this band overlapped the band region corresponding to the vibrations due to mannuronic and guluronic acid residues within alginate (Figs. S9 and S11, Table S4). This suggests that the decrease in intensity of this band region is likely related to the decrease in C content post-irradiation given that the other bands corresponding to alginate also decreased in intensity (Fig. S11). For post-irradiated Lp coprecipitates, specifically those with C/Fe 0.5 or 1.0, the position of their ν_{asym}(C-O-O) band shifted towards higher wavenumbers by ~7 and 5 cm^{-1}, respectively (Fig. S11). A slight decrease in intensity of the ν(O—H) band for the post-irradiated Lp coprecipitates with C/Fe ratio of 0.5 and 1.0 was also observed (Fig. S11). However, for both coprecipitates, the position of this band did not substantially change. In contrast, for the post-irradiated Lp coprecipitate with C/Fe ratio of 1.5 the intensity of the ν(O—H) did not change, but slightly shifted by ~6 cm^{-1} towards lower wavenumbers (Fig. S11). In addition to reduced intensity, the post-irradiated Lp coprecipitates exhibited broadening of the asymmetric band corresponding to the carboxylate functional group, also due to the appearance of a shoulder band as was observed with the post-irradiated Fh coprecipitates (Fig. S11).

Irradiation did not influence the mineralogy of pure Gt as the bands position and intensity were similar to those of the native Gt (Fig. S12). Similarly, the intensity, peak positions, and peak separation distance of the in-plane (δ(O—H)) and out of plane (γ(O—H)) vibrational bands, which are indicators of crystallinity (Schwertmann et al., 1985; Cornell and Schwertmann, 2003; Villacís-García et al., 2015), were comparable to those determined for the corresponding native controls. This suggests that irradiation did not affect the crystallinity of the Gt coprecipitates. In comparison to post-irradiated Fh and Lp coprecipitates, the IR spectra of the post-irradiated Gt coprecipitates did not exhibit substantial changes in the intensity or positions of the bands corresponding to ν(O—H) and alginate (Fig. S12).

3.5.3. ^{57}Fe Mössbauer spectroscopy

Mössbauer spectra collected at 77 and 5 K were used to characterize changes in the crystallinity and redox state of the post-irradiated Fhs relative to the native controls. The Mössbauer spectra of the native and irradiated Fhs are shown in Fig. 7, and the derived Mössbauer parameters are given in Table 1. In all spectra collected at 77 K, we observed a doublet with the parameter value of centre shift (CS): 0.35–0.5 mm/s and quadrupole split (QS): 0.7–0.85 mm/s, consistent with 2-line ferrihydrite. In spectra collected at 5 K, two sextets were observed: sextet A with parameters of CS = 0.48 mm/s, QS = 0 mm/s, hyperfine field (H) = 50 T, and sextet B with parameters of CS = 0.42 mm/s, QS = −0.03 mm/s, hyperfine field (H) = 45 T, consistent with ferrihydrite that is magnetically ordered at this temperature (Byrne and Kappler, 2022).

The post-irradiated Fhs show significant differences at both temperatures. All post-irradiation spectra collected at 77 K show a broadening of the Fe(III) doublet relative to the pre-irradiation spectra (Fig. 7). This broadening may be fit by the addition of a collapsed sextet with a low hyperfine field (5.4–20.6 T) and may indicate ferric oxyhydroxides that are partially ordered (Murad and Cashion, 2004; Byrne and Kappler, 2022). As this ferric oxyhydroxide phase shows ordering at 77 K while 2-line ferrihydrite does not, this phase may be more crystalline than ferrihydrite (Table 1). The 77 K spectrum of post-irradiated Fh coprecipitated with C/Fe ratio of 1.5 also exhibited an Fe(II) doublet with the parameters CS = 1.3 mm/s and QS = 2.7 (4.5% of the total spectral area) (Table 1).

The results of the spectra collected at 5 K are consistent with those collected at 77 K (Fig. 7). All spectra exhibit two sextets consistent with ferrihydrite. In the case of post-irradiated Fh coprecipitated with C/Fe ratio of 1.5, a small broadened Fe(II) doublet was added, consistent with the fits at 77 K (Fig. 7). It should be noted that the proportion of relative area of the Fe(II) doublet differ slightly between the 77 and the 5 K spectra as the proportion approaches the lower limit of detection of the Mössbauer (~2%) and is consistent with past observations of broadening of the Fe(II) doublet upon Fe(II) sorption to iron oxyhydroxides (Table 1) (Notini et al., 2019).

3.6. Bioavailability

Microbial Fe(III) reduction curves of the native and irradiated iron oxyhydroxides are presented in Fig. 8, which show the increase of total Fe(II) and dissolved Fe(II) relative to total Fe throughout the

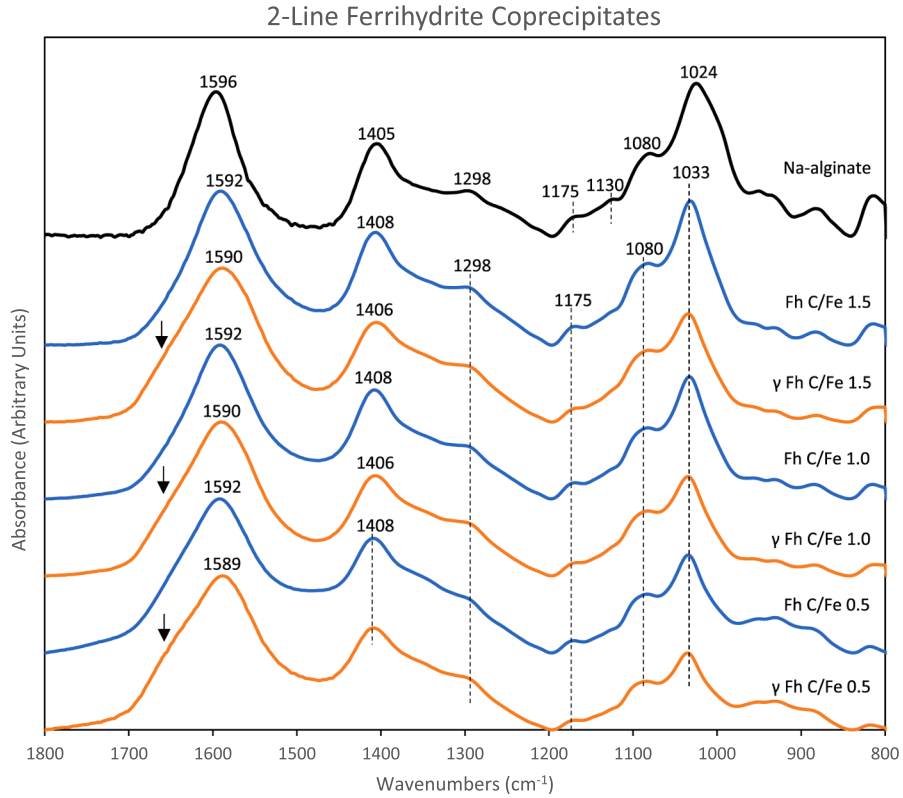

Fig. 6. FTIR spectra in the 1800–800 cm^{-1} region of 2-line ferrihydrite coprecipitated with alginate (C/Fe ratio of 0.5, 1.0, and 1.5 mol:mol) before and after γ-irradiation. The spectrum of Na-alginate was added for comparison. Notice the changes in intensity of the bands centred at ~1400 and 1030 cm^{-1} and the broadening of the band centred at ~1590 cm^{-1} following the irradiation treatment. Arrows point to the possible appearance of a shoulder band.

experimental period (up to 25 days). The rates of Fe(III) reduction by *S. putrefaciens* CN32 were calculated by linear regression of selected time points that corresponded to the period of maximum accumulation of total Fe(II) relative to total Fe (Fig. 8). The extent of Fe(III) reduction was determined from the maximum amount of total Fe(II) relative to total Fe, which equated to the average of the last 3 measurement points of an experiment ($n = 9$). A summary of the regression data and the maximum amount of Fe reduced for the native and post-irradiated iron oxyhydroxides are presented in Fig. 9 and Table S6. Control experiments showed no changes in the concentration of Fe(II) or pH throughout the experimental period, and their sterility was confirmed at the start and end of the experimental period (Fig. S13).

The overall trends in the distribution of Fe(II) throughout the microbial reduction of the post-irradiated iron oxyhydroxides were similar to those observed for their corresponding native controls (Fig. 8). However, a notable exception was found in the case of the post irradiated Fh coprecipitates, in which case a deviation in the extent of Fe reduction was observed at day 8 and gradually increased until termination of the experiment (Fig. 8). The post-irradiated Fh coprecipitates exhibited a 23–28% increase in the amount of Fe reduced compared to the native Fh coprecipitates (Fig. 9 and Table S6). Additionally, the extent of Fe(III) reduction among the irradiated Fh coprecipitates displayed significant variability based on C content ($P < 0.05$, one-way ANOVA), peaking at a C/Fe ratio of 1.0 (Fig. 9 and Table S6). However, relative to the irradiated Fh with C/Fe 0.5, the difference in the extent of Fe(III) reduction amounted to only ~5% (Fig. 9 and Table S6). Concurrently, with the release of biogenic Fe(II), pH also increased over the course of the experiment in the biotic systems (Fig. S13). It was observed that the pH reached higher values by 0.2–0.3 pH units during the microbial reduction of the post-irradiated Fh coprecipitates when compared to their corresponding native counterparts (Fig. S13). Despite these observations, however, the rate of Fe(III) reduction displayed no significant difference between the post-irradiated minerals and their corresponding native counterparts ($P > 0.05$, two tailed *t*-test, Fig. 9 and Table S6). Moreover, the concentrations of dissolved Fe(II) reached a similar proportion of the total Fe(II) as those measured for the corresponding native Fhs (Fig. 9).

In contrast to the Fh coprecipitates, the impact of irradiation on the reduction extent of the more crystalline Lp and Gt coprecipitates exhibited variability (Figs. 8 and 9). Significant deviations in the extent of Fe(III) reduction were only observed for the Lp and Gt coprecipitates, specifically in the cases of native Lp coprecipitated with a C/Fe ratio of 0.5 and native Gt coprecipitated with a C/Fe ratio of 1.5, when compared to their respective post-irradiated counterparts ($P < 0.05$, two tailed t-test). These differences accounted for approximately 10% and 8% variation, respectively (Fig. 9 and Table S6). The levels of pH also increased within the biotic systems, but in contrast to the Fh systems, the difference between the native and post-irradiated Lp and Gt coprecipitates was not as substantial (Figs. S14 and S15). Similar to the observations made for the Fh systems, the rates of Fe(III) reduction for the native Lp and Gt precipitates paralleled those determined for their respective irradiated counterparts (Fig. 9 and Table S6). Lastly, among all the post-irradiated Lps and Gts biotic microcosms, the concentrations of dissolved Fe(II) reached a comparable proportion of the total Fe(II) as measured for the corresponding native systems (Fig. 8).

3.6.1. *Biogenic solids*

X-ray diffractograms of the post-reduction minerals are shown in Figs. S16-S18. Broad reflections of residual Fh were observed in the biogenic solids after microbial reduction of native and irradiated Fhs (Fig. S16). Fe(III) reduction transformed pure native and post-irradiated Fh into Fh with slightly sharper reflections at 35 and 62°, indicating higher crystallinity (Fig. S16). However, no crystalline iron (oxyhydr) oxides such as goethite, lepidocrocite, or magnetite were detected in the

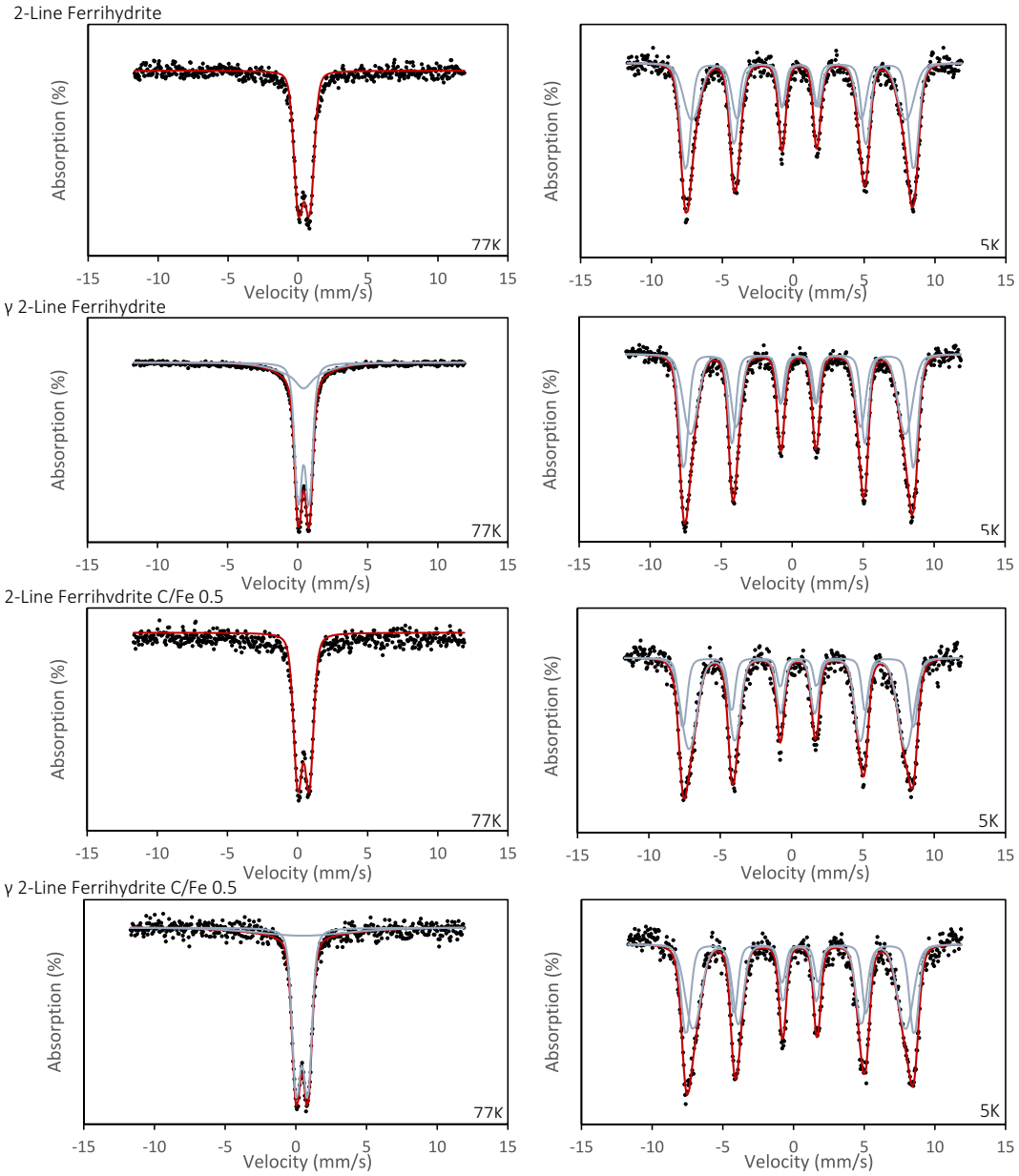

Fig. 7. Mössbauer spectra of native and post γ-irradiated 2-line ferrihydrites coprecipitated with alginate (C/Fe ratios of 0, 0.5, 1.0, and 1.5 mol:mol), taken at liquid nitrogen (77 K) and liquid helium temperature (5 K). Symbols show experimental data and lines represent their fit.

biogenic solids following the microbial reduction of the native and post-irradiated Fhs (Fig. S16). The addition of 400 μM phosphate led to vivianite ($Fe_3(PO_4)_2 \bullet 8H_2O$) precipitation in the biogenic solids from the native and post-irradiated pure Fh as well as post-irradiated Fh coprecipitates, but not from the native Fh coprecipitates (Fig. S16). Moreover, SEM and EDS analysis revealed plate-like morphologies rich in P and Fe, likely vivianite, where XRD confirmed its presence (Figs. S19-S22).

Microbial reduction of the native and irradiated Lps or Gts led to biogenic solids consisting mainly of residual Lp or Gt, respectively, together with vivianite, with no other differences (Figs. S17 and S18). SEM and EDS also confirmed the data observations made by XRD (Figs. S23 and S24). Interestingly, vivianite was absent from the biogenic solids from the native and irradiated Gt coprecipitated with C/Fe of 0.5 (Fig. S17).

4. Discussion

4.1. Effects of Na-alginate

The effects of γ-irradiation at a dose of 25 kGy on the physicochemical properties and bioavailability were tested on a range of synthetic iron oxyhydroxide minerals with variable thermodynamic stability and alginate content (C/Fe ratio of 0, 0.5, 1.0, and 1.5 mol:mol). Such effects were tested on minerals in the wet state since air-drying or freeze-drying significantly affects the aggregation state and reactivity of iron oxyhydroxides (Roden and Zachara, 1996; Raiswell et al., 2010). Coprecipitation of 2-line ferrihydrite (Fh), lepidocrocite (Lp), and goethite (Gt) with variable alginate content led to the precipitation of minerals with variable physicochemical properties, bioavailability, and therefore sensitivity. The effects of alginate content were evident through several analyses, including chemical extractions, measurements of porosity and SSA, XRD, FTIR spectroscopy, and the

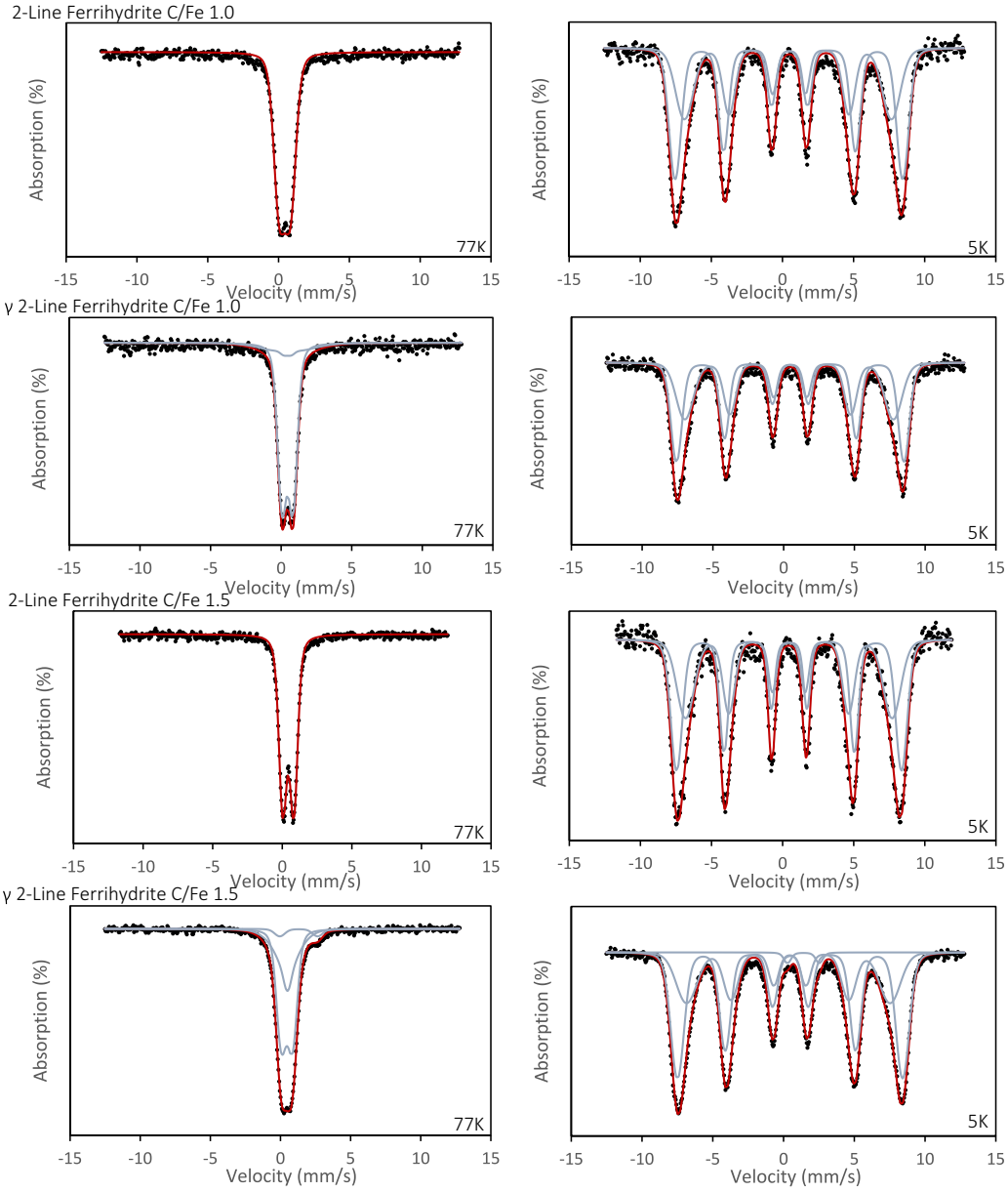

Fig. 7. (*continued*).

evaluation of bioavailability by *S. putrefaciens* CN32. Generally, coprecipitation with alginate led to the precipitation of minerals with lower crystallinity and smaller particle size as a consequence of alginate-induced poisoning of crystal growth, but with variable effects on the porosity and in turn on the SSA as well as bioavailability. These observations agree with past studies that have investigated the impact of organic substances, encompassing polysaccharides, humic and fulvic acids, as well as simple organic compounds, on the physicochemical properties of various synthetic iron oxyhydroxides (Liu and Huang, 2003; Schwertmann et al., 2005; Eusterhues et al., 2008; Mikutta et al., 2008; Shimizu et al., 2013; Chen et al., 2014; Poggenburg et al., 2016; Liu et al., 2019). Furthermore, the synthesized minerals exhibited similarities to the properties documented in literature for naturally occurring BIOS (Langley et al., 2009b; Toner et al., 2009; Gault et al., 2011; Najem et al., 2016; ThomasArrigo et al., 2022). Hence, the investigated iron oxyhydroxide minerals are of environmental relevance.

4.2. Impact of γ-irradiation: mineralogy

It is well established in the literature that the interaction of high energy γ-radiation with H_2O molecules leads to the production of a variety of primary and secondary radicals, and molecular products according to (Wren and Glowa, 2000; Joseph et al., 2008; Sutherland et al., 2017):

$$H_2O \xrightarrow{\gamma} e_{aq}^{-}, {}^{\bullet}H, {}^{\bullet}OH, H_2O_2, {}^{\bullet}HO_2, H_2, {}^{\bullet}O_2^{-}, \text{and } H_3O^{+} \quad (1)$$

Past and recent studies have exploited radiolysis products to investigate the formation of various iron oxyhydroxides using suspensions of dissolved ferrous iron, ferric iron, or ferric iron precipitates under various conditions (e.g. regarding pH and dissolved oxygen), and in the presence or absence of stabilizing agents (e.g. organic polymers) as well as $^{\bullet}OH$ scavengers (e.g. alcohols) under various doses of irradiation (Wang and Xin, 1999; Jurkin et al., 2011; Yakabuskie et al., 2011; Jurkin et al., 2016a; Jurkin et al., 2016b; Sutherland et al., 2017; Marić et al., 2019; Marić et al., 2020a; Marić et al., 2020b). Accordingly, the nature

Table 1
Mössbauer parameters for 2-line ferrihydrite and coprecipitates before and after γ-irradiation determined from spectra collected at liquid nitrogen (77 K) and liquid helium temperature (5 K).

Sample	T (K)	Site	CS (mm/s)	QS (mm/s)	H (T)	Relative area (%)	χ^2
Fh	77	Fe(III)	0.43	0.79		100	0.76
	5	Ferrihydrite A	0.46	−0.01	49.9	55.0	0.68
		Ferrihydrite B	0.44	−0.01	46.8	45.0	
γ Fh	77	Fe(III)	0.43	0.77		72.7	1.13
		Collapsed sextet	0.38	−0.05	10.6	27.3	
	5	Ferrihydrite A	0.46	0.0	50.1	48.7	0.79
		Ferrihydrite B	0.43	−0.02	46.9	51.3	
Fh C/Fe 0.5	77	Fe(III)	0.43	0.81		100	1.24
	5	Ferrihydrite A	0.48	0.0	50.2	30.0	0.70
		Ferrihydrite B	0.42	−0.01	47.1	70.0	
γ Fh C/Fe 0.5	77	Fe(III)	0.44	0.80		79.9	1.8
		Collapsed sextet	0.45	−0.05	20.7	20.1	
	5	Ferrihydrite A	0.46	0	50.0	39.9	0.71
		Ferrihydrite B	0.42	−0.02	46.6	60.1	
Fh C/Fe 1.0	77	Fe(III)	0.44	0.79		100	1.33
	5	Ferrihydrite A	0.48	−0.02	49.6	57.0	0.76
		Ferrihydrite B	0.42	−0.04	45.1	43.0	
γ Fh C/Fe 1.0	77	Fe(III)	0.45	0.78		86.4	0.84
		Collapsed sextet	0.45	0.00	10.8	13.6	
	5	Ferrihydrite A	0.47	0.00	49.8	54.0	0.76
		Ferrihydrite B	0.43	−0.04	45.7	46.0	
Fh C/Fe 1.5	77	Fe(III)	0.43	0.79		100	1.01
	5	Ferrihydrite A	0.45	0.00	49.1	54.0	0.68
		Ferrihydrite B	0.43	0.00	45.1	46.0	
γ Fh C/Fe 1.5	77	Fe(III)	0.46	0.80		63.4	0.75
		Fe(II)	1.3	2.7		4.5	
		Collapsed sextet	0.45	−0.05	5.4	32.1	
	5	Fe(II)	1.2	2.25		1.5	1.73
		Ferrihydrite A	0.47	−0.02	49.3	61.5	
		Ferrihydrite B	0.39	−0.05	44.6	37.0	

and concentration of the formed products depend on the dose rate, and conditions of the solution including temperature, pH, dissolved O_2 concentration, and solutes present in the system (Hochanadel and Ghormley, 1962; Joseph et al., 2008; Yakabuskie et al., 2011; Sutherland et al., 2017). Within neutral solutions with dissolved oxygen, initial reactions are likely driven by a range of oxidizing and reducing radicals including $^{\bullet}OH$, e^{-}_{aq}, and $^{\bullet}H$, and as the system rapidly reaches steady state, the contribution from H_2O_2 becomes more relevant as its concentration increases (Wren and Glowa, 2000; Joseph et al., 2008). Thus, in our systems, the radiolytic products react with each other, and available solutes leading to oxidation and reduction reactions as concurrent competitive processes. Upon irradiation of our systems, the reaction is initiated as rapid reduction of lattice ferric iron to ferrous iron according to:

$$Fe(III) + {e_{aq}}^{-} \rightarrow {Fe^{2+}}_{(aq)} \quad (2)$$

However, the mobility of Fe^{2+} is limited by rapid oxidation in solution and precipitation:

$${Fe^{2+}}_{(aq)} + OH^{\bullet} \rightarrow {Fe^{3+}}_{(aq)} + OH^{-} \quad (3)$$

$$Fe^{3+} + 3OH^{-} \leftrightarrows Fe(OH)^{2+} + 2OH^{-} \leftrightarrows Fe(OH)_2{}^{-} + OH^{-} \leftrightarrows Fe(OH)_3 \quad (4)$$

The mobility of Fe^{2+} is also limited by adsorption and subsequent oxidation by H_2O_2, according to:

$${Fe^{2+}}_{(aq)} \rightarrow {Fe(II)}_{ad} \quad (5)$$

$${Fe(II)}_{ad} + H_2O_2 \rightarrow 2{Fe(III)}_{ad} + 2OH^{-} \quad (6)$$

Thus, in the absence of alginate, reactions 3–6 limit the release of Fe^{2+} into solution, explaining the lack of measurable concentrations of this species in the supernatants of the post-irradiated pure minerals Fh, Lp, and Gt (Fig. 1). Moreover, the lack of changes of pH may indicate an equal production of protons and hydroxide ions (Fig. S2).

The cycle of concurrent radiolytically-induced reduction/oxidation reactions was also hypothesized to operate in a manner similar to Ostwald ripening, resulting in the coarsening of metal oxide nanoparticles through bridging and aggregation (Yakabuskie et al., 2011; Sutherland et al., 2017), which may eventually lead to transformation. This cycle may explain the observed increase in crystallinity of the Fhs in this study. Along the same lines, Brown et al. (2014) reported increased crystallite size and the partial transformation of 2-line ferrihydrite into a crystalline mineral phase resembling akageneite after irradiation to a total dose of 1 MGy. Their study suggested that the presence of trace amounts of Cl from the synthesis procedure, which involved neutralizing a $FeCl_3$ solution, could have facilitated the formation of akageneite. In a similar manner, the Fhs in our study were synthesized using a similar procedure. Hence, it is possible that the observed crystalline phase represents an intermediate state between akageneite and 2-line ferrihydrite, reflecting the findings of Brown et al. (2014). It is worth noting that the irradiated Fh coprecipitates exhibited similar changes in crystallinity compared to the irradiated pure Fh (Table 1). While no direct relationship was observed between the extent of the collapsed sextet at 77 K and alginate content, our results are intriguing, as the existing literature indicates that organic matter hinders the transformation of 2-line ferrihydrite into crystalline phases by binding particles and impeding dissolution-precipitation (goethite) and solid-state (hematite) conversion reactions (Cornell and Schwertmann, 2003; Chen et al., 2015; Najem et al., 2016). Nevertheless, despite the observed alterations in Fhs' crystallinity, they could not be distinguished through XRD, FTIR-ATR, chemical extractions, and, in the case of pure Fhs, their SSA and PV suggesting that at the first glance the irradiated Fhs and their native counterparts exhibit similar reactivity (Figs. 2 and 3).

In contrast to 2-line ferrihydrite, irradiation of a stable iron oxide phase such as hematite to a final dose of 1 MGy led to the partial formation of a poorly crystalline iron oxide phase (Brown et al., 2014). In our study, the fact that the extractable Fe fractions were comparable between the post-irradiated and native controls for pure Lp and Gt indicates that the possible formation of a poorly crystalline iron oxide phase is insignificant at the low dose (25 kGy) applied in this study (Fig. 2). Conversely, 0.5 M HCl extracted a lower amount of Fe from the post-irradiated Lp coprecipitates when compared to their native controls (Fig. 2). The reason for this is unknown, since we should expect the Gt coprecipitates to exhibit a similar trend (Fig. 2). However, the comparability of PV, SSA, together with ascorbate extractable Fe

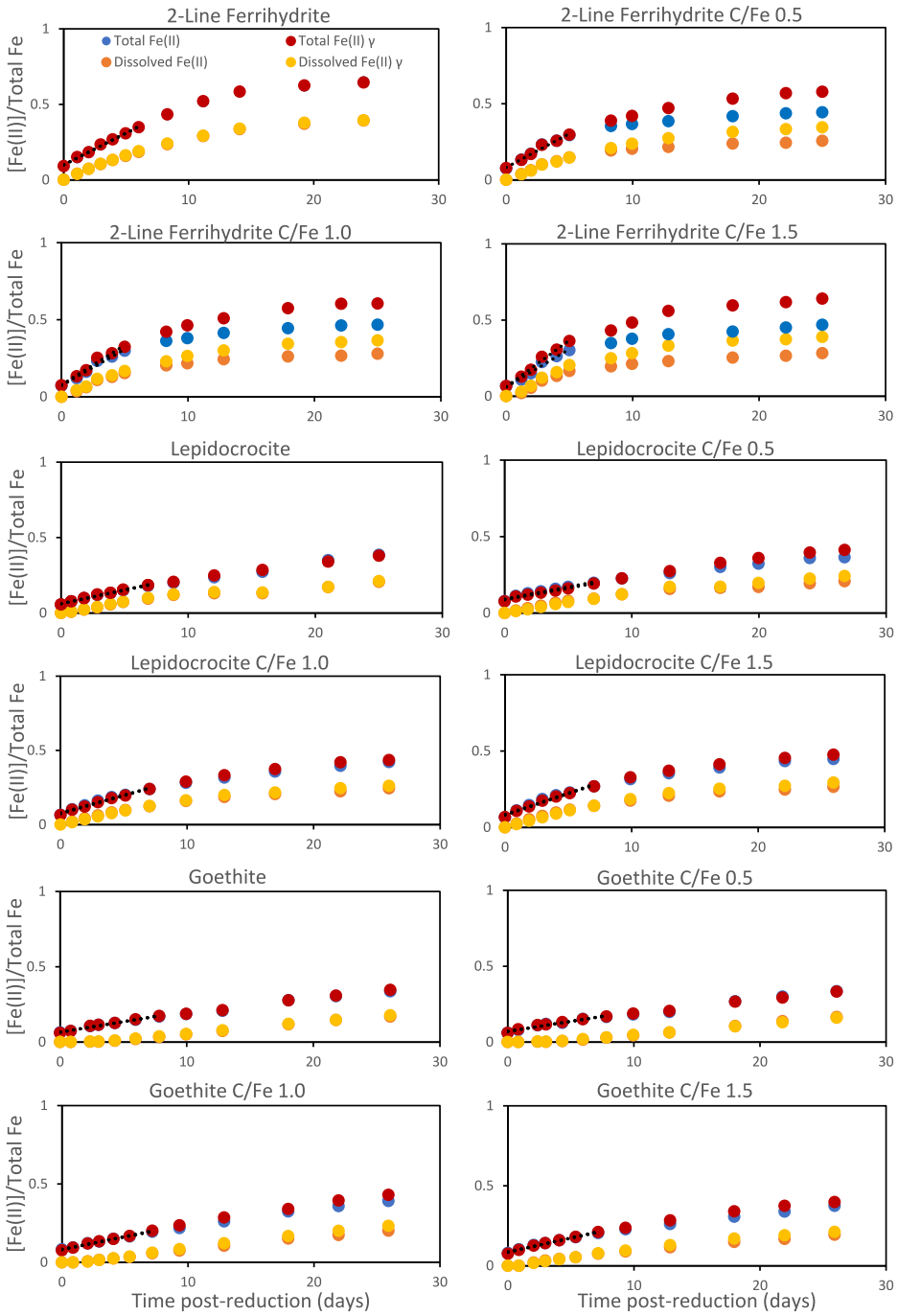

Fig. 8. Changes in total and dissolved Fe(II) relative to total Fe for native iron oxyhydroxides and their corresponding γ-irradiated counterparts during anaerobic Fe reduction by *S. putrefaciens* CN32. Dashed lines represent the maximum production of total Fe(II) from which the rate of Fe reduction was calculated. Data markers represent means ± standard deviations derived from three experimental replicates of each system.

measurements between the irradiated Lp and Gt coprecipitates and their native controls indicate minimal irradiation induced changes at their surface (Figs. 2 and 3).

4.3. Impact of γ-irradiation: role of Na-alginate

The presence of alginate in our systems adds another level of complexity. When exposed to irradiation, alginate undergoes degradation (Al-Assaf et al., 2016). Several studies have proposed the mechanism behind this degradation, which, in dilute solutions, initiates with the abstraction of H from the alginate chain by the radicals $^{\bullet}H$ and $^{\bullet}OH$ generated during the radiolysis of water (1) (Nagasawa et al., 2000; Wasikiewicz et al., 2005; Le Quang and Vo Thi, 2009; Al-Assaf et al., 2016). The alginate radicals are inherently unstable, leading to the cleavage of the 1,4-glycosidic bonds thereby reducing the molecular weight of alginate to form oligosaccharides and additional organic radicals through multiple pathways (Nagasawa et al., 2000; Wasikiewicz et al., 2005; Le Quang and Vo Thi, 2009; Al-Assaf et al., 2016). Indeed, irradiation of ≤1% alginate solutions, similar to the maximum alginate content in our jars, to a dose of 30 kGy led to a decrease in the molecular weight of alginate by ~96% (Nagasawa et al., 2000; Lee et al., 2003; Wasikiewicz et al., 2005). Degradation of alginate may also proceed by reaction with the radiolytically produced H_2O_2, however we expect this reaction to play a minor role given that the rate of this

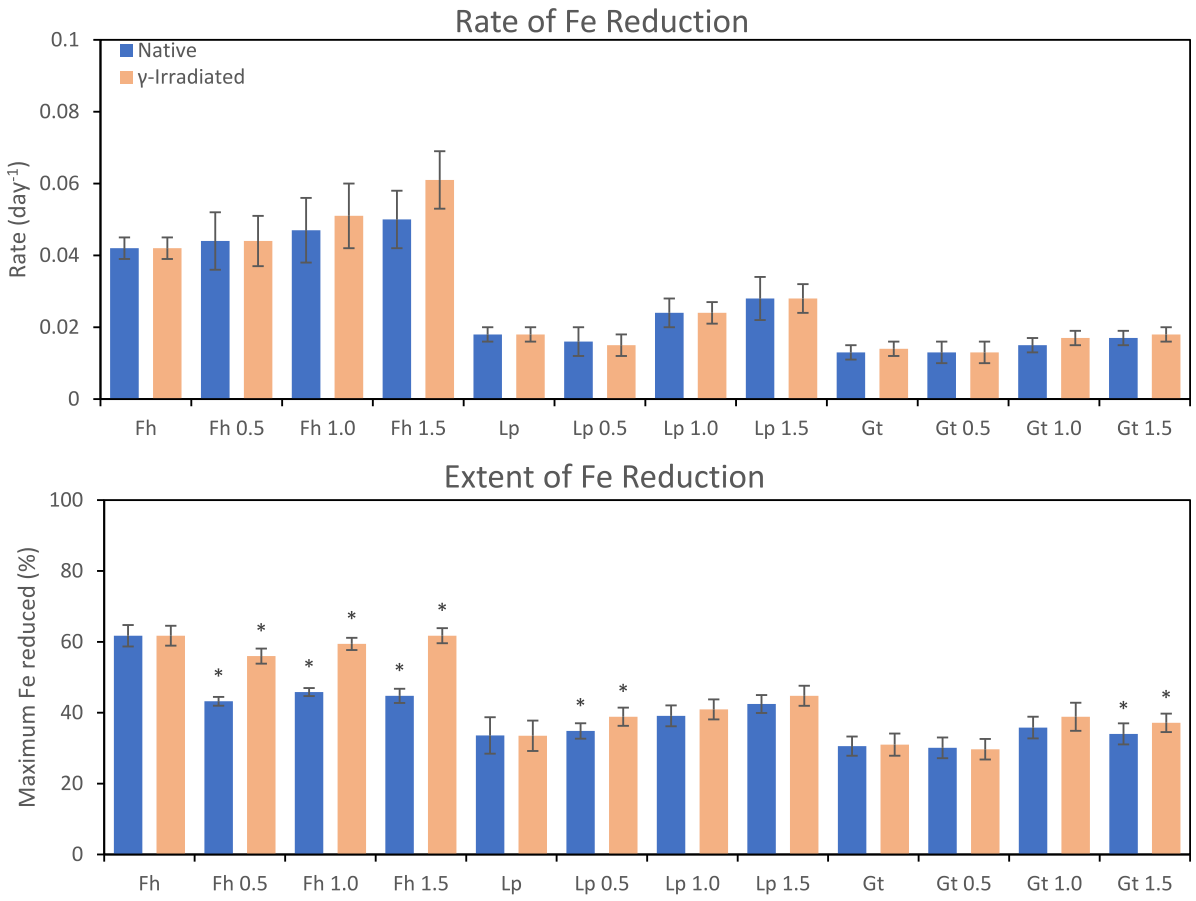

Fig. 9. Derived rate and extent of Fe(III) reduction of the native iron oxyhydroxides and their corresponding γ-irradiated counterparts. Data was collected from three individual experimental replicates for each system. Asterix indicates significant difference between the values at the 95% confidence interval ($P < 0.05$, two-tailed t-test). Fh, Lp, and Gt correspond to 2-line ferrihydrite, lepidocrocite, and goethite, respectively. Please see Table S6 for the numerical values.

reaction increases with increasing temperature (Li et al., 2010). Accompanying the decrease in molecular weight, studies have also reported the concomitant reduction in the viscosity of the alginate solutions, mirroring our observations for the post-irradiated coprecipitates, particularly for the Fh coprecipitates (Fig. S1) (Nagasawa et al., 2000; Lee et al., 2003; Wasikiewicz et al., 2005). This reduced viscosity likely explains the observed increased wet Fe content in the post-irradiated coprecipitates (Fig. 2).

The irradiation of the coprecipitates resulted in elevated levels of DOC, total dissolved Fe, and Fe(II) in the supernatants (Fig. 1). Notably, the absence of dissolved Fe species in the supernatants of post-irradiated pure iron oxyhydroxide phases, coupled with the apparent strong relationship between DOC and total dissolved Fe, provides compelling evidence for the role of alginate in promoting the dissolution of the coprecipitates during irradiation. FTIR-ATR analyses of the supernatants further confirmed the presence of alginate/alginate degradation products in solution (Figs. S25-S27). The IR spectra of the products collected from the supernatants of the post-irradiated coprecipitates exhibited some differences when compared to the IR spectra of Na-alginate or, where possible, the products collected from the supernatants of the corresponding native coprecipitates (Figs. S25-S27). Notably, the intensity of the band centered at ~1024–1030 cm^{-1}, presumed to correspond to the ν_{asym}(C-O-C) of the glycosidic linkage, was reduced relative to the intensity of the ν_{asym}(C-O-O) band centred at 1590–1592 cm^{-1}. Additionally, there was broadening and shifting of the ν_{asym}(C-O-O) band, centred at 1590–1592 cm^{-1}, by 4–6 cm^{-1} to lower wavenumbers (Figs. S25-S27). The former change could be attributed to the cleavage of the 1,4-glycosidic bonds in agreement with observations made by Le Quang and Vo Thi (2009), whereas the latter can be attributed to the complexation of the released Fe(III) by the carboxylate functional groups leading to changes in the local environment around these groups. The observed irradiation induced release of DOC into solution is in line with previous studies, which has been attributed to the breakdown of cellular biomass and carbohydrates by radicals, as described here for alginate (McNamara et al., 2003; Berns et al., 2008; Zhang et al., 2016; Otte et al., 2018). Moreover, the release of dissolved iron along with DOC corresponds to the findings of Schaller et al. (2011), who attributed this increase to the leaching of iron from microbial cells and/or organic/inorganic sediment particles.

The measurable amounts of Fe(II) detected in the supernatants of the post-irradiated coprecipitates indicate a reduction of lattice Fe that is likely mediated by the reducing radical, e^-_{aq}, as in reaction (2). However, it is apparent that alginate facilitated this reaction given that the concentration of dissolved Fe(II) increased with increasing initial concentration of alginate across all coprecipitates (Fig. 1). Structural reduction of Fe(III) to Fe(II) by irradiation to a dose of ~84 kGy was also apparent by Mössbauer spectroscopy in clay powders intercalated with simple alcohols (ethylene glycol and tert-butanol) (Gournis et al., 2000). The reduction was attributed to the hydrogen generated from the homolysis of the irradiated alcohols, whereas the generated alcohol radicals either dimerize or react with each other to generate stable molecules (Gournis et al., 2000). Alcohols may also facilitate the reduction of Fe(III) by maintaining a reducing environment, to some extent, by scavenging the $^{\bullet}$OH radical thereby hindering the oxidation of Fe(II) back to Fe(III) (Wang and Xin, 1999; Jurkin et al., 2016a; Jurkin et al., 2016b; Marić et al., 2020b). In our systems, alginate likely serves multiple roles. Firstly, alginate functions to stabilize and disperse iron oxide particles in solution thereby enhancing the contact between solid and liquid phase

upon irradiation and increasing the probability of contact with the irradiation generated reducing species (Wang and Xin, 1999; Gotić et al., 2009; Liu et al., 2009; Jurkin et al., 2011; Jurkin et al., 2016a; Marić et al., 2019; Marić et al., 2020b). Secondly, alginate and its degradation products function as scavengers for the oxidizing radical $^{\bullet}OH$ playing a role that is analogous to alcohols (Falkeborg et al., 2014). Thirdly, alginate and its degradation products bind Fe(II) and Fe(III) thereby providing further protection against oxidation and preventing the precipitation of new mixed Fe(II)/Fe(III) phases, respectively.

4.4. Impact of γ-irradiation: differences among the oxyhydroxides

The C content of the native coprecipitates increased with increasing initial alginate concentration, and at corresponding initial C/Fe ratio the final C content among the coprecipitates exhibited the following trend: Fh > > Lp ≥ Gt (Fig. 2). Therefore, synthesis of Fh via neutralization of acidic Fe(III) solution led to a higher uptake of alginate as opposed to synthesis via Fe(II) oxidation and subsequent Fe(III) hydrolysis pathway for Lp and Gt (Fig. 2). The C/Fe ratio for the Fh coprecipitates ranged from 0.5 to 1.5, whereas it varied from 0.24 to 0.64 for Lp coprecipitates and from 0.24 to 0.44 for Gt coprecipitates (Fig. 2). Consequently, Lp and Gt that were coprecipitated with an initial C/Fe ratio of 1.0 or 1.5 retained a C/Fe ratio that is equivalent to- or close to- that of Fh coprecipitated with a C/Fe ratio of 0.5 (Fig. 2). The former synthesis procedure also led to the formation of larger aggregates as determined by particle size analyses such that at corresponding initial C/Fe ratios, the native Fh coprecipitates exhibited the largest particle sizes among the studied coprecipitates (Fig. 4). Moreover, for the native Fh with a C/Fe ratio of 0.5, the particles exhibited a pH_{iep} of ~6.6, which decreased to <4 as the C/Fe ratio increased to 1.0 and 1.5 (Fig. S6). In contrast, all of the native Lp and Gt coprecipitates exhibited a pH_{iep} of <4 (Figs. S7 and S8). The different synthesis pathways of the studied minerals also led to different changes in PV and SSA (Fig. 3). With increasing alginate content, the SSA of the Fh coprecipitates decreased, while the SSA of the Lp coprecipitates increased, whereas the SSA of the Gt coprecipitates decreased (Fig. 3). Consequently, given the distinct mineralogy and physicochemical properties among the synthetic coprecipitates, it is not surprising that they would exhibit a varying response to the irradiation treatment.

For instance, changes in the PV and SSA were detected only in the post-irradiated Fh coprecipitates with a C/Fe ratio of 0.5 and 1.0 (Fig. 3). The observed changes induced by irradiation could be attributed to the modification of the coprecipitates' surface that is likely associated with the release of DOC and Fe. These modifications are evidenced by the ζ-potential measurements for these minerals (Fig. S6). For Fh with C/Fe ratio of 0.5, the C content did not change post-irradiation, and the amount of DOC in solution accounted for ~2% of the initial total C pool (Figs. 1 and 2). This amount was considerably lower when compared to the amount of DOC measured following the irradiation of Fh coprecipitated with C/Fe ratios of 1.0 or 1.5 (Fig. 1). This observation could be attributed to the re-adsorption of the negatively charged alginate products to the surface of the Fh particles as evidenced by the decrease of pH_{iep} for this mineral (Fig. S6). Adsorption proceeds at the surface of Fh thereby blocking the pores and in turn reducing the SSA as was determined for this mineral (Fig. 3). This reaction may also explain the observed decline in the PV and SSA for the post-irradiated Fh coprecipitated with a C/Fe ratio of 1.0, whereas the PV and SSA for post-irradiated Fh coprecipitated with a C/Fe ratio of 1.5 could not be assessed by N_2-adsorption as a consequence of the already blocked pores by alginate (Fig. 3). For the latter coprecipitates, their surface charge became more positive relative to their corresponding native counterparts, which could be attributed to charge neutralization by the adsorption of Fe(III) (Fig. S6). Modifications to the surface of the post-irradiated Fh coprecipitates could be also reflected by the observed changes to the FTIR-ATR spectra (Fig. 6). Notably, broadening of the bands corresponding to the carboxylate functional groups indicative of changes in the local environment around these groups as was observed for the supernatants post-irradiation (Fig. S25).

In contrast to the Fh coprecipitates, the PV and SSA of the Lp and Gt coprecipitates did not change post-irradiation, even at equivalent or near equivalent C/Fe ratios to Fh coprecipitated with a C/Fe ratio of 0.5 (Fig. 3). Moreover, their surface charge remained comparable to that of their native counterparts, whereas irradiation induced changes to the particle size were only evident among the Lp coprecipitates as opposed to the Gt coprecipitates (Fig. 4). Likewise, irradiation induced surface modifications as highlighted by changes to the local environment around the carboxylate function groups were only evident among the Lp coprecipitates as opposed to the Gt coprecipitates (Fig. S11). The apparent difference in the extent of irradiation induced changes between the Lp and Gt coprecipitates could be attributed to the higher poorly crystalline Fe fraction of the former as determined by the 0.5 M HCl and ascorbate chemical extractions (Fig. 2). This poorly crystalline Fe fraction coprecipitated with alginate may be more susceptible to irradiation induced degradation than the crystalline phases such as Gt. However, despite the apparent similarity of changes in the discussed physicochemical properties of the Lp coprecipitates to those observed for the Fh coprecipitates, the lack of changes to PV and SSA of the former coprecipitates, especially at the highest C/Fe contents, is unknown and warrants further investigation. Likewise, the reason for the lack of irradiation induced changes to the physiochemical properties of the Gt coprecipitates in comparison to Lp and Fh coprecipitates is unknown. However, it remains possible that the difference in synthesis pathways may have resulted in variations in the distribution and arrangement of alginate within the coprecipitates. Such notion may explain the different response of the coprecipitates to the irradiation treatment.

4.5. Impact of γ-irradiation: bioavailability

In addition to the analytical techniques employed in this study, microbial Fe(III) reduction experiments were carried out to further probe the impact of γ-irradiation on the bioavailability (rate and extent of Fe reduction) of the various iron oxyhydroxides studied (Figs. 8 and 9, Table S6). It is very well established in the literature that the rate and extent of Fe(III) reduction by Fe(III) reducing bacteria (FeRB) is dictated by several factors, including: cell concentration (O'Loughlin et al., 2010), SSA (Roden and Zachara, 1996; Roden, 2003), particle aggregation (Roden and Zachara, 1996; Roden, 2003; Cutting et al., 2009), crystallinity and morphology (Cutting et al., 2009), solubility (Bonneville et al., 2004; Bonneville et al., 2009), Fe(II) concentration (Roden and Zachara, 1996; Fredrickson et al., 1998; Roden and Urrutia, 2002), the presence of simple organic ligands (Urrutia et al., 1999; O'Loughlin et al., 2010), and redox-active molecules (e.g. electron shuttles) (Jiang and Kappler, 2008). In the case of Fe-OM precipitates, additional factors control the bioavailability of Fe and these include: the mode of association between the mineral and OM (i.e. adsorption vs. coprecipitation) (Eusterhues et al., 2014; Kleber et al., 2015), type of OM (Poggenburg et al., 2016), C/Fe molar ratio (Shimizu et al., 2013; Eusterhues et al., 2014; Adhikari et al., 2017), surface charge (Amstaetter et al., 2012), extent of OM induced aggregation (Amstaetter et al., 2012; Adhikari et al., 2016; Poggenburg et al., 2016; Poggenburg et al., 2018), and the orientation of the experimental vessels (Dippon et al., 2015). In the current study, it was observed that the initial cell counts for a biotic system using both a native and a corresponding post-irradiated iron oxyhydroxide were comparable within the margin of error (Table S7). This observation indicates that any variations observed in the rate or extent of Fe(III) reduction can be confidently attributed to differences associated with the physicochemical properties of the mineral phases.

SSA is commonly employed as a quantitative measure to assess the availability of reactive sites for FeRB (Roden and Zachara, 1996; Roden, 2003). Therefore, this parameter can serve as an indicator of the potential bioavailability of iron oxyhydroxides, with an increase in SSA generally favouring microbial Fe(III) reduction, and conversely, a

decrease impeding it (Roden and Zachara, 1996; Roden, 2003). In the case of the Fh coprecipitates with a C/Fe ratio of 0.5 or 1.0, we observed a reduction in SSA following the irradiation treatment (Fig. 3). As a result, one might expect that the bioavailability of those minerals would be lower than that of their corresponding native controls. However, the rates of Fe(III) reduction for those minerals were comparable, while the extent of Fe(III) reduction was noticeably higher for the irradiated Fh coprecipitates compared to their native controls (Figs. 8 and 9, Table S6). This suggests that SSA alone is an unreliable predictor of mineral bioavailability, especially in the context of Fe-OM-coprecipitates (Mikutta and Kretzschmar, 2008; Mikutta et al., 2008; Chen et al., 2014; Poggenburg et al., 2016; Poggenburg et al., 2018). Our findings align with those of several other studies (Mikutta and Kretzschmar, 2008; Langley et al., 2009c; Langley et al., 2009d; Poggenburg et al., 2016), and suggest that other factors control the bioavailability of the studied minerals.

An increased rate of Fe(III) reduction by *Shewanella oneidensis* MR-1 was reported for 2-line ferrihydrite post-irradiation to a dose of 1 MGy (Brown et al., 2014). Furthermore, the rate and extent of Fe(III) reduction were doubled in the presence of an electron shuttle (riboflavin) (Brown et al., 2014). This enhancement was attributed to the partial transformation of ferrihydrite into an akageneite-like phase, and reduced aggregation of ferrihydrite particles (Brown et al., 2014). While we observed a similar partial conversion of Fh into a phase with higher crystallinity following irradiation, the rate and extent of reduction for the irradiated Fh were found to be comparable to that of the native control (Figs. 8 and 9, Table S6). Additionally, we found that the particle size of the irradiated Fh aggregates in suspension was similar to that of the native control (Fig. 4). Consequently, the lower dosage used in this study (25 kGy) did not appear to significantly affect the aggregation state of Fh particles, as opposed to the high dosage applied by Brown et al. (2014). Similarly, the bioavailability of pure Lp and Gt did not change post-irradiation (Figs. 8 and 9, Table S6), consistent with the lack of alterations in their bulk mineralogy, PV, SSA, particle size, and poorly crystalline Fe fraction as determined by chemical extractions compared to their native controls. Brown et al. (2014) observed that in the absence of an electron shuttle, there was no difference in the bioavailability between irradiated (1 MGy) and native hematite, despite the irradiation induced partial transformation of the mineral into a poorly crystalline Fe (III) phase. However, a difference was observed only when an electron shuttle (riboflavin) was present. Therefore, the addition of an electron shuttle, combined with spectroscopic analyses, might reveal a different outcome for these minerals (Lp and Gt).

In contrast to pure ferrihydrite, the aggregation state of the post-irradiated coprecipitates differed from that of the native controls (Fig. 4). When the coprecipitates were suspended in the chemically defined medium, we observed variations in the stability of the aggregates (Fig. S28). Specifically, the native Fh coprecipitates appeared to form large aggregates that settled quickly at the bottom of the microcosm bottles. In contrast, the irradiated Fh coprecipitates appeared to form both stable suspensions and larger aggregates, probably due to irradiation-induced degradation of alginate. This observation became more apparent throughout the experimentation period (Fig. S28), and measurements of particle size further corroborated our findings (Fig. 4). This observation might elucidate the difference in the extent of reduction for the post-irradiated ferrihydrite coprecipitates compared to their native controls (Figs. 8 and 9, Table S6). Larger aggregates would impede the accessibility for the bacteria to available sites, whereas the smaller aggregates would increase site accessibility (Amstaetter et al., 2012; Adhikari et al., 2017). Furthermore, the similarity of the particle size among the post-irradiated Fh coprecipitates likely explains their comparability of the extent of Fe(III) reduction (Figs. 4 and 9). It is also possible that as Fe reduction progresses, the aggregation state of the coprecipitates undergoes changes due to the release and re-adsorption of alginate, a process that may differ between alginate and alginate oligosaccharides.

The particle size of the Lp coprecipitates similarly decreased after irradiation, and yet the degree of microbial Fe reduction in comparison to their native counterparts was not as substantial as seen for the Fh coprecipitates (Fig. 4). However, it is also possible that distinctions may become more apparent over a longer time period, exceeding 25 days, due to the slower rates of Fe(III) reduction of the Lp coprecipitates (Fig. 8). The difference in the extent of Fe(III) reduction between the native and post-irradiated Gt coprecipitates was also not as substantial as seen for the Fh coprecipitates (Fig. 8). The lack of changes in the particle size for the Gt coprecipitates might account for the similarity of bioavailability between the irradiated and native coprecipitates for Gt coprecipitates.

In addition to OM controlling the aggregation state and thus the bioavailability of iron oxyhydroxide coprecipitates, OM, depending on the C/Fe ratio and type, may also enhance the bioavailability of iron oxyhydroxides through multiple pathways. Enhancement may proceed through (1) the alleviation of the thermodynamic constraint from the buildup of enzymatically generated Fe(II) on the oxyhydroxide surface (Fredrickson et al., 1998; Urrutia et al., 1999; Roden, 2003; Hyacinthe et al., 2006), and (2) the stabilization of thermodynamically unstable minerals, particularly Fh and Lp, against Fe(II)-catalyzed transformation into minerals that are less susceptible to microbial Fe(III) reduction, such as magnetite or goethite (Fredrickson et al., 1998; Zachara et al., 2002; Kleber et al., 2015). However, alginate and alginate oligosaccharides exhibit a limited capacity to chelate Fe(II) (Falkeborg et al., 2014). Among the minerals studied, this is further emphasized by the similar proportion of dissolved Fe(II) in relation to total Fe(II) between a native and its corresponding post-irradiated coprecipitate, which also matches that of a corresponding pure phase (Fig. 8).

4.6. Characterization of bioreduced solids

The specific identity of biogenic minerals formed during Fe(III) reduction depends on various factors including: the stability of the iron oxide phase (Fredrickson et al., 1998; Cutting et al., 2009), Fe(II) concentration and rate of release (Fredrickson et al., 1998; Hansel et al., 2003; Amstaetter et al., 2012), solution's chemistry (e.g. buffer type and PO_4 concentration) (Fredrickson et al., 1998; Zachara et al., 2002; Borch et al., 2007), OM content (Shimizu et al., 2013; Chen et al., 2015; Poggenburg et al., 2016; Adhikari et al., 2017), and the orientation of the microcosm vessel (Dippon et al., 2015). The absence of crystalline phases in our Fh experiments is partly due to phosphate, which inhibits goethite and magnetite formation by binding to Fh surfaces and forming vivianite and Fe(II) complexes (Hansel et al., 2003; Borch et al., 2007; Amstaetter et al., 2012). Experimental work at our laboratory indicated that at a concentration of 400 μM, phosphate is fully adsorbed by the native Fhs studied (data not shown). Thus, vivianite precipitation occurs as Fe(III) reduction exceeds the adsorption capacity of a mineral phase towards phosphate (Fig. 8). However, irradiation induced changes to the surface area of Fh coprecipitates (C/Fe 0.5 and C/Fe 1.0) may have reduced their capacity to adsorb phosphate, thereby allowing for vivianite to reach saturation and precipitate.

In addition to phosphate, OM also contributes to stabilizing Fh against transformation (Cornell and Schwertmann, 2003; Kleber et al., 2015). OM has been shown to hinder surface interactions with Fe(II), thereby reducing the rate of electron transfer between Fe(II) and Fe(III) necessary for the formation of goethite and magnetite (Amstaetter et al., 2012; Shimizu et al., 2013; Chen et al., 2015). Furthermore, OM can alter the pathway of mineral transformation, a property that is dependent on the C/Fe ratio (Shimizu et al., 2013; Chen et al., 2015; Adhikari et al., 2017). At a high C/Fe ratio of 4.3, Shimizu et al. (2013) postulated that the aggregation of Fh-OM-coprecipitates created microenvironments that limited the diffusion of Fe(II) and HCO_3^- into the solution, effectively trapping these species and creating favourable conditions for the precipitation of green rust. However, considering the influence of irradiation on aggregate stability and the reduction of the C content in

the Fh coprecipitates, it leads us to hypothesize that irradiation might lead to erroneous conclusions regarding the pathways of mineral transformation and the specific minerals that may form in natural samples.

5. Conclusions

In this study, we found that γ-irradiation to a total dose of 25 kGy led to significant reduction and dissolution of synthetic iron oxyhydroxides coprecipitated with varying concentrations of Na-alginate. The extent of such reactions was found to increase with increasing alginate content. Our results may explain the observations made by Schaller et al. (2011) who reported a significant release of DOC and a concomitant release of Fe and Mn as well as U and As following irradiation of organic rich sediments. Irradiation was also found to have a significant impact on the physicochemical and mineralogical properties of Fh coprecipitates (C/Fe 0.5, 1.0, and 1.5). The observed irradiation induced decrease in SSA and aggregation of these coprecipitates may lead to over-or-underestimation of the adsorption capacity of a natural sample towards contaminants and nutrients (e.g. As, P, Cu). Likewise, enhanced bioavailability may lead to erroneous conclusions regarding the extent of Fe reduction and organic matter release, which has important implications for research relevant to C cycling that is associated with the iron oxyhydroxide mineral fractions.

We attempted to investigate the impact of irradiation on the physicochemical properties of iron oxyhydroxides with variable thermodynamic stability to reflect those occurring in natural samples, including BIOS (Gault et al., 2011; ThomasArrigo et al., 2022). Synthesis of such minerals required the use of variable synthesis procedures that led to the formation of minerals with distinct physicochemical properties as a consequence of the variations in the distribution and arrangement of alginate within the coprecipitates. Consequently, whether the observed irradiation-induced changes, particularly in Fh coprecipitates, accurately reflect those found in natural samples or are solely attributable to the chosen synthesis pathway, remains uncertain. For example, whether or not Fh that is synthesized in the absence of Cl (e.g. $Fe(NO_3)_3$) will undergo similar changes in crystallinity remains to be determined in future studies.

For this research, we opted for Na-alginate as the representative organic compound, because the impact of irradiation on this polysaccharide is well characterized in the literature (Le Quang and Vo Thi, 2009). However, it is important to note that the impact of irradiation varies with OM type and stability, which may lead to soil/sediment specific effects (Da Silva et al., 1997; Zhao et al., 2020; Zhao et al., 2021). Moreover, the chemistry of the natural sample plays an important role in modulating the impact of irradiation due to the presence of redox sensitive compounds capable of scavenging the reducing and oxidizing radicals (Cataldo and Angelini, 2012; Brown et al., 2015). In addition to this consideration, it is important to note that the response of OM to irradiation is dose-dependent (Da Silva et al., 1997; Zhao et al., 2020). Consequently, irradiation induced changes to Fe-coprecipitates may become more apparent at higher doses.

Finally, the results from this study could be also relevant to deep geological repository (DGR) environments where spent fuel is intended to be stored (Brown et al., 2015; Zhao et al., 2021; Zhao et al., 2022a), and deep subsurface environments (Blair et al., 2007). Within such conditions where radioactive decay fuels the flux of γ-radiation may enhance the dissolution of Fe-OM-coprecipitates and the microbial reduction of Fe(III). Nonetheless, from a sterilization point of view, our results indicate that γ-irradiation induced physicochemical changes to the minerals tested which is contrary to numerous other studies identifying γ-sterilization as a minimally invasive technique. Therefore, future researchers must be cognizant of the potential effects of sterilization through γ-irradiation on Fe-OM-coprecipitates.

CRediT authorship contribution statement

Tarek Najem: Writing – review & editing, Writing – original draft, Visualization, Validation, Methodology, Investigation, Formal analysis, Data curation, Conceptualization. **Prachi Joshi:** Writing – review & editing, Visualization, Methodology, Formal analysis, Data curation. **Andreas Kappler:** Writing – review & editing, Validation, Resources, Methodology. **Danielle Fortin:** Writing – review & editing, Validation, Supervision, Resources, Project administration, Funding acquisition, Conceptualization.

Declaration of competing interest

The authors declare that they have no known competing financial interests or personal relationships that could have appeared to influence the work reported in this paper.

Data availability

Raw data for data from this manuscript and supplementary materials are available through Mendeley Data: https://data.mendeley.com/datasets/ycw92c3ywy/1

Acknowledgements

The present research was entirely funded by a NSERC Discovery grant to D. Fortin. The authors are very thankful to Nordion (Canada) Inc. for sterilizing our samples. We are grateful to 2 anonymous reviewers and the editor for their very constructive comments. We would like to thank Nimal DeSilva and Smita Mohanty (University of Ottawa) for their expertise and analyzing our samples with the ICP-OES, the Ján *V*eizer Stable Isotope Lab (University of Ottawa) for their expertise and analysis of DOC and carbon content, and Dr. Javier Giorgi (University of Ottawa) for providing the access and training to use the Autosorb-1 for sample analysis. We would also like to thank Glenn Poirier (University of Ottawa) for his guidance and expertise in using the SEM.

Appendix A. Supplementary data

Supplementary data to this article can be found online at https://doi.org/10.1016/j.chemgeo.2024.122235.

References

Adhikari, D., Poulson, S.R., Sumaila, S., Dynes, J.J., McBeth, J.M., Yang, Y., 2016. Asynchronous reductive release of iron and organic carbon from hematite–humic acid complexes. Chem. Geol. 430, 13–20.

Adhikari, D., Zhao, Q., Das, K., Mejia, J., Huang, R., Wang, X., Poulson, S.R., Tang, Y., Roden, E.E., Yang, Y., 2017. Dynamics of ferrihydrite-bound organic carbon during microbial Fe reduction. Geochim. Cosmochim. Acta 212, 221–233.

Al-Assaf, S., Coqueret, X., Zaman, H.M.D.K., Sen, M., Ulański, P., 2016. The Radiation Chemistry of Polysaccharides. International Atomic Energy Agency Vienna, Austria.

Amstaetter, K., Borch, T., Kappler, A., 2012. Influence of humic acid imposed changes of ferrihydrite aggregation on microbial Fe (III) reduction. Geochim. Cosmochim. Acta 85, 326–341.

Bank, T.L., Kukkadapu, R.K., Madden, A.S., Ginder-Vogel, M.A., Baldwin, M.E., Jardine, P.M., 2008. Effects of gamma-sterilization on the physico-chemical properties of natural sediments. Chem. Geol. 251 (1–4), 1–7.

Bao, Y., Bolan, N.S., Lai, J., Wang, Y., Jin, X., Kirkham, M.B., Wu, X., Fang, Z., Zhang, Y., Wang, H., 2021. Interactions between organic matter and Fe (hydr)oxides and their influences on immobilization and remobilization of metal(loid)s: a review. Crit. Rev. Environ. Sci. Technol. 52 (22), 4016–4037.

Berns, A.E., Philipp, H., Narres, H.D., Burauel, P., Vereecken, H., Tappe, W., 2008. Effect of gamma-sterilization and autoclaving on soil organic matter structure as studied by solid state NMR, UV and fluorescence spectroscopy. Eur. J. Soil Sci. 59 (3), 540–550.

Blair, C.C., D'Hondt, S., Spivack, A.J., Kingsley, R.H., 2007. Radiolytic hydrogen and microbial respiration in subsurface sediments. Astrobiology 7 (6), 951–970.

Bonneville, S., Van Cappellen, P., Behrends, T., 2004. Microbial reduction of iron (III) oxyhydroxides: effects of mineral solubility and availability. Chem. Geol. 212 (3–4), 255–268.

Bonneville, S., Behrends, T., Van Cappellen, P., 2009. Solubility and dissimilatory reduction kinetics of iron (III) oxyhydroxides: a linear free energy relationship. Geochim. Cosmochim. Acta 73 (18), 5273–5282.
Borch, T., Masue, Y., Kukkadapu, R.K., Fendorf, S., 2007. Phosphate imposed limitations on biological reduction and alteration of ferrihydrite. Environ. Sci. Technol. 41 (1), 166–172.
Borisover, M., Keren, Y., Usyskin, A., Bukhanovsky, N., 2016. Effects of gamma-irradiation of original and organic matter-amended soils on the sorption of triclosan and diuron from aqueous solutions. Chemosphere 152, 62–70.
Brown, A.R., Wincott, P.L., LaVerne, J.A., Small, J.S., Vaughan, D.J., Pimblott, S.M., Lloyd, J.R., 2014. The impact of gamma radiation on the bioavailability of Fe(III) minerals for microbial respiration. Environ. Sci. Technol. 48 (18), 10672–10680.
Brown, A.R., Boothman, C., Pimblott, S.M., Lloyd, J.R., 2015. The impact of gamma radiation on sediment microbial processes. Appl. Environ. Microbiol. 81 (12), 4014–4025.
Buchan, D., Moeskops, B., Ameloot, N., De Neve, S., Sleutel, S., 2012. Selective sterilisation of undisturbed soil cores by gamma irradiation: Effects on free-living nematodes, microbial community and nitrogen dynamics. Soil Biol. Biochem. 47, 10–13.
Buessecker, S., Tylor, K., Nye, J., Holbert, K.E., Urquiza Muñoz, J.D., Glass, J.B., Hartnett, H.E., Cadillo-Quiroz, H., 2019. Effects of sterilization techniques on chemodenitrification and N_2O production in tropical peat soil microcosms. Biogeosciences 16 (23), 4601–4612.
Byrne, J.M., Kappler, A., 2022. A revised analysis of ferrihydrite at liquid helium temperature using Mössbauer spectroscopy. Am. Mineral. 107 (8), 1643–1651.
Cardenas-Jiron, G., Leal, D., Matsuhiro, B., Osorio-Roman, I.O., 2011. Vibrational spectroscopy and density functional theory calculations of poly-D-mannuronate and heteropolymeric fractions from sodium alginate. J. Raman Spectrosc. 42 (4), 870–878.
Cataldo, F., Angelini, G., 2012. Radiolysis and ozonolysis of a landfill leachate. Radioanal. Nucl. Chem. 293 (1), 141–148.
Chan, C.S., De Stasio, G., Welch, S.A., Girasole, M., Frazer, B.H., Nesterova, M.V., Fakra, S., Banfield, J.F., 2004. Microbial polysaccharides template assembly of nanocrystal fibers. Science 303 (5664), 1656–1658.
Chan, C.S., Fakra, S.C., Edwards, D.C., Emerson, D., Banfield, J.F., 2009. Iron oxyhydroxide mineralization on microbial extracellular polysaccharides. Geochim. Cosmochim. Acta 73 (13), 3807–3818.
Chandıa, N., Matsuhiro, B., Vásquez, A., 2001. Alginic acids in Lessonia trabeculata: characterization by formic acid hydrolysis and FT-IR spectroscopy. Carbohydr. Polym. 46 (1), 81–87.
Chen, C., Dynes, J.J., Wang, J., Sparks, D.L., 2014. Properties of Fe-organic matter associations via coprecipitation versus adsorption. Environ. Sci. Technol. 48 (23), 13751–13759.
Chen, C., Kukkadapu, R., Sparks, D.L., 2015. Influence of Coprecipitated Organic Matter on Fe^{2+}(aq)-Catalyzed Transformation of Ferrihydrite: Implications for Carbon Dynamics. Environ. Sci. Technol. 49 (18), 10927–10936.
Chen, K.-Y., Hsu, L.-C., Chan, Y.-T., Cho, Y.-L., Tsao, F.-Y., Tzou, Y.-M., Hsieh, Y.-C., Liu, Y.-T., 2018. Phosphate removal in relation to structural development of humic acid-iron coprecipitates. Sci. Rep. 8 (1), 10363.
Cismasu, A.C., Michel, F.M., Tcaciuc, A.P., Tyliszczak, T., Brown, J.G.E., 2011. Composition and structural aspects of naturally occurring ferrihydrite. Compt. Rendus Geosci. 343 (2–3), 210–218.
Cismasu, A.C., Williams, K.H., Nico, P.S., 2016. Iron and Carbon Dynamics during Aging and Reductive Transformation of Biogenic Ferrihydrite. Environ. Sci. Technol. 50 (1), 25–35.
Cooper, R.E., Eusterhues, K., Wegner, C.-E., Totsche, K.U., Küsel, K., 2017. Ferrihydrite-associated organic matter (OM) stimulates reduction by Shewanella oneidensis MR-1 and a complex microbial consortia. Biogeosciences 14 (22), 5171–5188.
Cornell, R.M., Schwertmann, U., 2003. The iron Oxides: Structure, Properties, Reactions, Occurrences, and Uses, 664. Wiley-vch Weinheim.
Curti, L., Moore, O.W., Babakhani, P., Xiao, K.-Q., Woulds, C., Bray, A.W., Fisher, B.J., Kazemian, M., Kaulich, B., Peacock, C.L., 2021. Carboxyl-richness controls organic carbon preservation during coprecipitation with iron (oxyhydr)oxides in the natural environment. Commun. Earth Environ. 2 (1).
Cutting, R., Coker, V., Fellowes, J., Lloyd, J., Vaughan, D., 2009. Mineralogical and morphological constraints on the reduction of Fe (III) minerals by Geobacter sulfurreducens. Geochim. Cosmochim. Acta 73 (14), 4004–4022.
Da Silva, W., Da Silva, S., de Oliveira Rezende, M., 1997. Influence of gamma-radiation on the behavior of humic acids from peat and tropical soil. Radioanal. Nucl. Chem. 222, 29–34.
Dippon, U., Schmidt, C., Behrens, S., Kappler, A., 2015. Secondary mineral formation during ferrihydrite reduction by Shewanella oneidensis MR-1 depends on incubation vessel orientation and resulting gradients of cells, Fe^{2+} and Fe minerals. Geomicrobiol J. 32 (10), 878–889.
Dong, H., Huang, L., Zhao, L., Zeng, Q., Liu, X., Sheng, Y., Shi, L., Wu, G., Jiang, H., Li, F., Zhang, L., Guo, D., Li, G., Hou, W., Chen, H., 2022. A critical review of mineral–microbe interaction and co-evolution: mechanisms and applications. Natl. Sci. Rev. 9 (10).
Dong, H., Zeng, Q., Sheng, Y., Chen, C., Yu, G., Kappler, A., 2023. Coupled iron cycling and organic matter transformation across redox interfaces. Nature Rev. Earth & Environ. 4 (9), 659–673.
Eusterhues, K., Wagner, F.E., Häusler, W., Hanzlik, M., Knicker, H., Totsche, K.U., Kögel-Knabner, I., Schwertmann, U., 2008. Characterization of ferrihydrite-soil organic matter coprecipitates by X-ray diffraction and Mossbauer spectroscopy. Environ. Sci. Technol. 42 (21), 7891–7897.
Eusterhues, K., Hädrich, A., Neidhardt, J., Küsel, K., Keller, T., Jandt, K., Totsche, K., 2014. Reduction of ferrihydrite with adsorbed and coprecipitated organic matter: microbial reduction by Geobacter bremensis vs. abiotic reduction by Na-dithionite. Biogeosciences 11 (18), 4953–4966.
Fabisch, M., Freyer, G., Johnson, C.A., Buchel, G., Akob, D.M., Neu, T.R., Kusel, K., 2016. Dominance of 'Gallionella capsiferriformans' and heavy metal association with Gallionella-like stalks in metal-rich pH 6 mine water discharge. Geobiology 14 (1), 68–90.
Falkeborg, M., Cheong, L.-Z., Gianfico, C., Sztukiel, K.M., Kristensen, K., Glasius, M., Xu, X., Guo, Z., 2014. Alginate oligosaccharides: Enzymatic preparation and antioxidant property evaluation. Food Chem. 164, 185–194.
Field, H.R., Whitaker, A.H., Henson, J.A., Duckworth, O.W., 2019. Sorption of copper and phosphate to diverse biogenic iron (oxyhydr) oxide deposits. Sci. Total Environ. 697, 134111.
Fortin, D., Langley, S., 2005. Formation and occurrence of biogenic iron-rich minerals. Earth Sci. Rev. 72 (1–2), 1–19.
Fredrickson, J.K., Zachara, J.M., Kennedy, D.W., Dong, H., Onstott, T.C., Hinman, N.W., Li, S.-M., 1998. Biogenic iron mineralization accompanying the dissimilatory reduction of hydrous ferric oxide by a groundwater bacterium. Geochim. Cosmochim. Acta 62 (19–20), 3239–3257.
Gault, A.G., Ibrahim, A., Langley, S., Renaud, R., Takahashi, Y., Boothman, C., Lloyd, J. R., Clark, I.D., Ferris, F.G., Fortin, D., 2011. Microbial and geochemical features suggest iron redox cycling within bacteriogenic iron oxide-rich sediments. Chem. Geol. 281 (1–2), 41–51.
Glasauer, S., Weidler, P.G., Langley, S., Beveridge, T.J., 2003. Controls on Fe reduction and mineral formation by a subsurface bacterium. Geochim. Cosmochim. Acta 67 (7), 1277–1288.
Goraczko, W., Slawinski, J., 2008. Luminescence from γ-irradiated humic acid. JOL 128 (7), 1155–1161.
Goraczko, W., Slawiński, J., Staninski, K., 2008. Spectral distribution of the radiochemiluminescence from gamma-irradiated humic acid. Radioanal. Nucl. Chem. 277 (3), 613–618.
Gotić, M., Jurkin, T., Musić, S., 2009. From iron(III) precursor to magnetite and vice versa. Mater. Res. Bull. 44 (10), 2014–2021.
Gournis, D., Mantaka-Marketou, A., Karakassides, M., Petridis, D., 2000. Effect of γ-irradiation on clays and organoclays: a Mössbauer and XRD study. Phys. Chem. Miner. 27, 514–521.
Grybos, M., Davranche, M., Gruau, G., Petitjean, P., 2007. Is trace metal release in wetland soils controlled by organic matter mobility or Fe-oxyhydroxides reduction? J. Colloid Interface Sci. 314 (2), 490–501.
Han, L., Sun, K., Keiluweit, M., Yang, Y., Yang, Y., Jin, J., Sun, H., Wu, F., Xing, B., 2019. Mobilization of ferrihydrite-associated organic carbon during Fe reduction: Adsorption versus coprecipitation. Chem. Geol. 503, 61–68.
Hansel, C.M., Benner, S.G., Neiss, J., Dohnalkova, A., Kukkadapu, R.K., Fendorf, S., 2003. Secondary mineralization pathways induced by dissimilatory iron reduction of ferrihydrite under advective flow. Geochim. Cosmochim. Acta 67 (16), 2977–2992.
Hao, L., Guo, Y., Byrne, J.M., Zeitvogel, F., Schmid, G., Ingino, P., Li, J., Neu, T.R., Swanner, E.D., Kappler, A., Obst, M., 2016. Binding of heavy metal ions in aggregates of microbial cells, EPS and biogenic iron minerals measured in-situ using metal- and glycoconjugates-specific fluorophores. Geochim. Cosmochim. Acta 180, 66–96.
Henneberry, Y.K., Kraus, T.E.C., Nico, P.S., Horwath, W.R., 2012. Structural stability of coprecipitated natural organic matter and ferric iron under reducing conditions. Org. Geochem. 48, 81–89.
Herbert, R.B., Malmström, M., Ebenå, G., Salmon, U., Ferrow, E., Fuchs, M., 2005. Quantification of abiotic reaction rates in mine tailings: evaluation of treatment methods for eliminating iron-and sulfur-oxidizing bacteria. Environ. Sci. Technol. 39 (3), 770–777.
Hochanadel, C., Ghormley, J., 1962. Effect of temperature on the decomposition of water by gamma rays. Radiat. Res. 16 (5), 653–660.
Hyacinthe, C., Bonneville, S., Van Cappellen, P., 2006. Reactive iron(III) in sediments: Chemical versus microbial extractions. Geochim. Cosmochim. Acta 70 (16), 4166–4180.
Jiang, J., Kappler, A., 2008. Kinetics of microbial and chemical reduction of humic substances: implications for electron shuttling. Environ. Sci. Technol. 42 (10), 3563–3569.
Joseph, J.M., Seon Choi, B., Yakabuskie, P., Clara Wren, J., 2008. A combined experimental and model analysis on the effect of pH and O_2(aq) on γ-radiolytically produced H_2 and H_2O_2. Radiat. Phys. Chem. 77 (9), 1009–1020.
Jurkin, T., Zadro, K., Gotić, M., Musić, S., 2011. Investigation of solid phase upon γ-irradiation of ferrihydrite-ethanol suspension. Radiat. Phys. Chem. 80 (7), 792–798.
Jurkin, T., Gotić, M., Štefanić, G., Pucić, I., 2016a. Gamma-irradiation synthesis of iron oxide nanoparticles in the presence of PEO, PVP or CTAB. Radiat. Phys. Chem. 124, 75–83.
Jurkin, T., Štefanić, G., Dražić, G., Gotić, M., 2016b. Synthesis route to δ-FeOOH nanodiscs. Mater. Lett. 173, 55–59.
Kaiser, K., 2003. Sorption of natural organic matter fractions to goethite (α-FeOOH): effect of chemical composition as revealed by liquid-state ^{13}C NMR and wet-chemical analysis. Org. Geochem. 34 (11), 1569–1579.
Kaiser, K., Guggenberger, G., Haumaier, L., Zech, W., 1997. Dissolved organic matter sorption on sub soils and minerals studied by ^{13}C-NMR and DRIFT spectroscopy. Eur. J. Soil Sci. 48 (2), 301–310.
Kaiser, K., Mikutta, R., Guggenberger, G., 2007. Increased stability of organic matter sorbed to ferrihydrite and goethite on aging. Soil Sci. Soc. Am. J. 71 (3), 711–719.

Kallenbach, C.M., Frey, S.D., Grandy, A.S., 2016. Direct evidence for microbial-derived soil organic matter formation and its ecophysiological controls. Nat. Commun. 7 (1), 13630.
Kelsey, J.W., Slizovskiy, I.B., Peters, R.D., Melnick, A.M., 2010. Sterilization affects soil organic matter chemistry and bioaccumulation of spiked p,p'-DDE and anthracene by earthworms. Environ. Pollut. 158 (6), 2251–2257.
Kleber, M., Eusterhues, K., Keiluweit, M., Mikutta, C., Mikutta, R., Nico, P.S., 2015. Mineral–Organic Associations: Formation, Properties, and Relevance in Soil Environments, 130, pp. 1–140.
Kostka, J.E., Luther, G.W., 1994. Partitioning and speciation of solid phase iron in saltmarsh sediments. Geochim. Cosmochim. Acta 58 (7), 1701–1710.
Lagarec, K., Rancourt, D.G., 1997. Extended Voigt-based analytic lineshape method for determining N-dimensional correlated hyperfine parameter distributions in Mössbauer spectroscopy. Nucl. Instrum. Methods Phys. Res., Sect. B 129 (2), 266–280.
Lalonde, K., Mucci, A., Ouellet, A., Gélinas, Y., 2012. Preservation of organic matter in sediments promoted by iron. Nature 483 (7388), 198–200.
Langley, S., Gault, A., Ibrahim, A., Renaud, R., Fortin, D., Clark, I.D., Ferris, F.G., 2009a. A comparison of the rates of Fe(III) reduction in synthetic and bacteriogenic iron oxides by shewanella putrefaciens CN32. Geomicrobiol J. 26 (2), 57–70.
Langley, S., Gault, A., Ibrahim, A., Renaud, R., Fortin, D., Clark, I.D., Ferris, F.G., 2009b. A comparison of the rates of Fe(III) reduction in synthetic and bacteriogenic iron oxides byshewanella putrefaciensCN32. Geomicrobiol J. 26 (2), 57–70.
Langley, S., Gault, A.G., Ibrahim, A., Takahashi, Y., Renaud, R., Fortin, D., Clark, I.D., Ferris, F.G., 2009c. Strontium desorption from bacteriogenic iron oxides (BIOS) subjected to microbial Fe(III) reduction. Chem. Geol. 262 (3–4), 217–228.
Langley, S., Igric, P., Takahashi, Y., Sakai, Y., Fortin, D., Hannington, M.D., Schwarz-Schampera, U., 2009d. Preliminary characterization and biological reduction of putative biogenic iron oxides (BIOS) from the Tonga-Kermadec Arc, Southwest Pacific Ocean. Geobiology 7 (1), 35–49.
Layglon, N., Misson, B., Mounier, S., Lenoble, V., Omanovic, D., Garnier, C., 2020. Have decades of abiotic studies in sediments been misinterpreted? Sci. Total Environ. 707, 135949.
Le Quang, L., Vo Thi, T.H., 2009. A study of degradation mechanism of alginate by gamma-irradiation. Radioisotopes 58 (1), 1–11.
Leal, D., Matsuhiro, B., Rossi, M., Caruso, F., 2008. FT-IR spectra of alginic acid block fractions in three species of brown seaweeds. Carbohydr. Res. 343 (2), 308–316.
Lee, D.W., Choi, W.S., Byun, M.W., Park, H.J., Yu, Y.-M., Lee, C.M., 2003. Effect of γ-irradiation on degradation of alginate. J. Agric. Food Chem. 51 (16), 4819–4823.
Lees, K., Fitzsimons, M., Snape, J., Tappin, A., Comber, S., 2018. Soil sterilisation methods for use in OECD 106: how effective are they? Chemosphere 209, 61–67.
Lensi, R., Lescure, C., Steinberg, C., Savoie, J.-M., Faurie, G., 1991. Dynamics of residual enzyme activities, denitrification potential, and physico-chemical properties in a γ-sterilized soil. Soil Biol. Biochem. 23 (4), 367–373.
Li, X., Xu, A., Xie, H., Yu, W., Xie, W., Ma, X., 2010. Preparation of low molecular weight alginate by hydrogen peroxide depolymerization for tissue engineering. Carbohydr. Polym. 79 (3), 660–664.
Li, Q., Hu, W., Li, L., Li, Y., 2023. Interactions between organic matter and Fe oxides at soil micro-interfaces: quantification, associations, and influencing factors. Sci. Total Environ. 855, 158710.
Liu, C., Huang, P., 2003. Kinetics of lead adsorption by iron oxides formed under the influence of citrate. Geochim. Cosmochim. Acta 67 (5), 1045–1054.
Liu, Y., Chen, S., Zhong, L., Wu, G., 2009. Preparation of high-stable silver nanoparticle dispersion by using sodium alginate as a stabilizer under gamma radiation. Radiat. Phys. Chem. 78 (4), 251–255.
Liu, Q., Li, X., Tang, J., Zhou, Y., Lin, Q., Xiao, R., Zhang, M., 2019. Characterization of goethite-fulvic acid composites and their impact on the immobility of Pb/Cd in soil. Chemosphere 222, 556–563.
Lotrario, J., Stuart, B., Lam, T., Arands, R., O'Connor, O., Kosson, D., 1995. Effects of sterilization methods on the physical characteristics of soil: implications for sorption isotherm analyses. Bull. Environ. Contam. Toxicol. 54, 668–675.
Marić, I., Štefanić, G., Gotić, M., Jurkin, T., 2019. The impact of dextran sulfate on the radiolytic synthesis of magnetic iron oxide nanoparticles. J. Mol. Struct. 1183, 126–136.
Marić, I., Dražić, G., Štefanić, G., Zadro, K., Gotić, M., Jurkin, T., 2020a. Characterization of radiolytically synthesized feroxyhyte and oxidized magnetite nanoparticles. Mater. Charact. 159, 110038.
Marić, I., Gotić, M., Štefanić, G., Pustak, A., Jurkin, T., 2020b. γ-Irradiation generated ferrous ions affect the formation of magnetite and feroxyhyte. Radiat. Phys. Chem. 170, 108648.
Martens, J., Mueller, C.W., Joshi, P., Rosinger, C., Maisch, M., Kappler, A., Bonkowski, M., Schwamborn, G., Schirrmeister, L., Rethemeyer, J., 2023. Stabilization of mineral-associated organic carbon in Pleistocene permafrost. Nat. Commun. 14 (1), 2120.
McNamara, N.P., Black, H.I.J., Beresford, N.A., Parekh, N.R., 2003. Effects of acute gamma irradiation on chemical, physical and biological properties of soils. Appl. Soil Ecol. 24 (2), 117–132.
Mejia, J., He, S., Yang, Y., Ginder-Vogel, M., Roden, E.E., 2018. Stability of ferrihydrite-humic acid coprecipitates under iron-reducing conditions. Environ. Sci. Technol. 52 (22), 13174–13183.
Mikutta, C., Kretzschmar, R., 2008. Synthetic coprecipitates of exopolysaccharides and ferrihydrite. Part II: Siderophore-promoted dissolution. Geochim. Cosmochim. Acta 72 (4), 1128–1142.
Mikutta, C., Mikutta, R., Bonneville, S., Wagner, F., Voegelin, A., Christl, I., Kretzschmar, R., 2008. Synthetic coprecipitates of exopolysaccharides and ferrihydrite. Part I: Characterization. Geochim. Cosmochim. Acta 72 (4), 1111–1127.
Mikutta, R., Lorenz, D., Guggenberger, G., Haumaier, L., Freund, A., 2014. Properties and reactivity of Fe-organic matter associations formed by coprecipitation versus adsorption: Clues from arsenate batch adsorption. Geochim. Cosmochim. Acta 144, 258–276.
Murad, E., Cashion, J., 2004. Mössbauer Spectroscopy of Environmental Materials and their Industrial Utilization. Springer Science & Business Media.
Nagasawa, N., Mitomo, H., Yoshii, F., Kume, T., 2000. Radiation-induced degradation of sodium alginate. Polym. Degrad. Stab. 69 (3), 279–285.
Najem, T., Langley, S., Fortin, D., 2016. A comparison of Fe(III) reduction rates between fresh and aged biogenic iron oxides (BIOS) by Shewanella putrefaciens CN32. Chem. Geol. 439, 1–12.
Notini, L., Latta, D.E., Neumann, A., Pearce, C.I., Sassi, M., N'Diaye, A.T., Rosso, K.M., Scherer, M.M., 2019. A closer look at Fe (II) passivation of goethite. ACS Earth Space Chem. 3 (12), 2717–2725.
O'Loughlin, E.J., Gorski, C.A., Scherer, M.M., Boyanov, M.I., Kemner, K.M., 2010. Effects of oxyanions, natural organic matter, and bacterial cell numbers on the bioreduction of lepidocrocite (γ-FeOOH) and the formation of secondary mineralization products. Environ. Sci. Technol. 44 (12), 4570–4576.
Otte, J.M., Blackwell, N., Soos, V., Rughoft, S., Maisch, M., Kappler, A., Kleindienst, S., Schmidt, C., 2018. Sterilization impacts on marine sediment—Are we able to inactivate microorganisms in environmental samples? FEMS Microbiol. Ecol. 94 (12).
Patzner, M.S., Logan, M., McKenna, A.M., Young, R.B., Zhou, Z., Joss, H., Mueller, C.W., Hoeschen, C., Scholten, T., Straub, D., Kleindienst, S., Borch, T., Kappler, A., Bryce, C., 2022. Microbial iron cycling during palsa hillslope collapse promotes greenhouse gas emissions before complete permafrost thaw. Commun. Earth Environ. 3 (1).
Pedrot, M., Le Boudec, A., Davranche, M., Dia, A., Henin, O., 2011. How does organic matter constrain the nature, size and availability of Fe nanoparticles for biological reduction? J. Colloid Interface Sci. 359 (1), 75–85.
Plötze, M., Kahr, G., Hermanns Stengele, R., 2003. Alteration of clay minerals—gamma-irradiation effects on physicochemical properties. Appl. Clay Sci. 23 (1–4), 195–202.
Poggenburg, C., Mikutta, R., Sander, M., Schippers, A., Marchanka, A., Dohrmann, R., Guggenberger, G., 2016. Microbial reduction of ferrihydrite-organic matter coprecipitates by Shewanella putrefaciens and Geobacter metallireducens in comparison to mediated electrochemical reduction. Chem. Geol. 447, 133–147.
Poggenburg, C., Mikutta, R., Schippers, A., Dohrmann, R., Guggenberger, G., 2018. Impact of natural organic matter coatings on the microbial reduction of iron oxides. Geochim. Cosmochim. Acta 224, 223–248.
Possinger, A.R., Zachman, M.J., Dynes, J.J., Regier, T.Z., Kourkoutis, L.F., Lehmann, J., 2021. Co-precipitation induces changes to iron and carbon chemistry and spatial distribution at the nanometer scale. Geochim. Cosmochim. Acta 314, 1–15.
Radloff, K.A., Manning, A.R., Mailloux, B., Zheng, Y., Rahman, M.M., Huq, M.R., Ahmed, K.M., van Geen, A., 2008. Considerations for conducting incubations to study the mechanisms of as release in reducing groundwater aquifers. Appl. Geochem. 23 (11), 3224–3235.
Raiswell, R., Vu, H.P., Brinza, L., Benning, L.G., 2010. The determination of labile Fe in ferrihydrite by ascorbic acid extraction: Methodology, dissolution kinetics and loss of solubility with age and de-watering. Chem. Geol. 278 (1–2), 70–79.
Retelletti Brogi, S., Derrien, M., Hur, J., 2019. In-depth assessment of the effect of sodium azide on the optical properties of dissolved organic matter. J. Fluoresc. 29 (4), 877–885.
Riedel, T., Zak, D., Biester, H., Dittmar, T., 2013. Iron traps terrestrially derived dissolved organic matter at redox interfaces. Proc. Natl. Acad. Sci. 110 (25), 10101–10105.
Roden, E.E., 2003. Fe (III) oxide reactivity toward biological versus chemical reduction. Environ. Sci. Technol. 37 (7), 1319–1324.
Roden, E.E., Urrutia, M.M., 2002. Influence of biogenic Fe (II) on bacterial crystalline Fe (III) oxide reduction. Geomicrobiol J. 19 (2), 209–251.
Roden, E.E., Zachara, J.M., 1996. Microbial reduction of crystalline iron (III) oxides: influence of oxide surface area and potential for cell growth. Environ. Sci. Technol. 30 (5), 1618–1628.
Rouquerol, J., Llewellyn, P., Rouquerol, F., 2007. Is the BET equation applicable to microporous adsorbents. Stud. Surf. Sci. Catal. 160 (07), 49–56.
Salonius, P., Robinson, J., Chase, F., 1967. A comparison of autoclaved and gamma-irradiated soils as media for microbial colonization experiments. Plant Soil 27 (2), 239–248.
Sartori, C., Finch, D.S., Ralph, B., Gilding, K., 1997. Determination of the cation content of alginate thin films by FTIR spectroscopy. Polymer 38 (1), 43–51.
Schaller, J., Weiske, A., Dudel, E.G., 2011. Effects of gamma-sterilization on DOC, uranium and arsenic remobilization from organic and microbial rich stream sediments. Sci. Total Environ. 409 (17), 3211–3214.
Schwertmann, U., Cornell, R.M., 2008. Iron Oxides in the Laboratory: Preparation and Characterization. John Wiley & Sons.
Schwertmann, U., Cambier, P., Murad, E., 1985. Properties of goethites of varying crystallinity. Clay Clay Miner. 33, 369–378.
Schwertmann, U., Wagner, F., Knicker, H., 2005. Ferrihydrite–Humic Associations. Soil Sci. Soc. Am. J. 69 (4), 1009–1015.
Seder-Colomina, M., Mangeret, A., Bauda, P., Brest, J., Stetten, L., Merrot, P., Julien, A., Diez, O., Barker, E., Billoir, E., Poupin, P., Thouvenot, A., Cazala, C., Morin, G., 2022. Influence of microorganisms on uranium release from mining-impacted lake sediments under various oxygenation conditions. Environ Sci Process Impacts 24 (10), 1830–1843.
Shimizu, M., Zhou, J., Schroder, C., Obst, M., Kappler, A., Borch, T., 2013. Dissimilatory reduction and transformation of ferrihydrite-humic acid coprecipitates. Environ. Sci. Technol. 47 (23), 13375–13384.

Skulcova, L., Scherr, K.E., Chrast, L., Hofman, J., Bielska, L., 2018. Influence of soil gamma-irradiation and spiking on sorption of p,p'-DDE and soil organic matter chemistry. Ecotoxicol. Environ. Saf. 155, 125–132.
Slizovskiy, I.B., Kelsey, J.W., 2010. Soil sterilization affects aging-related sequestration and bioavailability of p,p'-DDE and anthracene to earthworms. Environ. Pollut. 158 (10), 3285–3289.
Sowers, T.D., Harrington, J.M., Polizzotto, M.L., Duckworth, O.W., 2017. Sorption of arsenic to biogenic iron (oxyhydr) oxides produced in circumneutral environments. Geochim. Cosmochim. Acta 198, 194–207.
Stookey, L.L., 1970. Ferrozine—a new spectrophotometric reagent for iron. Anal. Chem. 42 (7), 779–781.
Sutherland, T., Sparks, C., Joseph, J., Wang, Z., Whitaker, G., Sham, T., Wren, J., 2017. Effect of ferrous ion concentration on the kinetics of radiation-induced iron-oxide nanoparticle formation and growth. Phys. Chem. Chem. Phys. 19 (1), 695–708.
ThomasArrigo, L.K., Notini, L., Shuster, J., Nydegger, T., Vontobel, S., Fischer, S., Kappler, A., Kretzschmar, R., 2022. Mineral characterization and composition of Fe-rich flocs from wetlands of Iceland: Implications for Fe, C and trace element export. Sci. Total Environ. 816, 151567.
Toner, B.M., Santelli, C.M., Marcus, M.A., Wirth, R., Chan, C.S., McCollom, T., Bach, W., Edwards, K.J., 2009. Biogenic iron oxyhydroxide formation at mid-ocean ridge hydrothermal vents: Juan de Fuca Ridge. Geochim. Cosmochim. Acta 73 (2), 388–403.
Tourney, J., Ngwenya, B.T., 2014. The role of bacterial extracellular polymeric substances in geomicrobiology. Chem. Geol. 386, 115–132.
Tuominen, L., Kairesalo, T., Hartikainen, H., 1994. Comparison of methods for inhibiting bacterial activity in sediment. Appl. Environ. Microbiol. 60 (9), 3454–3457.
Urrutia, M.M., Roden, E.E., Zachara, J.M., 1999. Influence of aqueous and solid-phase Fe (II) complexants on microbial reduction of crystalline iron (III) oxides. Environ. Sci. Technol. 33 (22), 4022–4028.
Villacís-García, M., Ugalde-Arzate, M., Vaca-Escobar, K., Villalobos, M., Zanella, R., Martínez-Villegas, N., 2015. Laboratory synthesis of goethite and ferrihydrite of controlled particle sizes. Bol. Soc. Geol. Mex. 67 (3), 433–446.
Viollier, E., Inglett, P.W., Hunter, K., Roychoudhury, A.N., Van Cappellen, P., 2000. The ferrozine method revisited: Fe(II)/Fe(III) determination in natural waters. Appl. Geochem. 15 (6), 785–790.
Wagai, R., Mayer, L.M., 2007. Sorptive stabilization of organic matter in soils by hydrous iron oxides. Geochim. Cosmochim. Acta 71 (1), 25–35.
Wang, S., Xin, H., 1999. The γ-irradiation-induced chemical change from β-FeOOH to Fe_3O_4. Radiat. Phys. Chem. 56 (5–6), 567–572.
Wasikiewicz, J.M., Yoshii, F., Nagasawa, N., Wach, R.A., Mitomo, H., 2005. Degradation of chitosan and sodium alginate by gamma radiation, sonochemical and ultraviolet methods. Radiat. Phys. Chem. 73 (5), 287–295.
Wehr, J.B., Kirchhof, G., 2021. Gamma irradiation with 50 kGy has a limited effect on agronomic properties of air-dry soil. Soil syst. 5 (2), 28.
Wolf, D., Dao, T., Scott, H., Lavy, T., 1989. Influence of Sterilization Methods on Selected Soil Microbiological, Physical, and Chemical Properties, 0047-2425,. Wiley Online Library.
Wren, J.C., Glowa, G.A., 2000. A simplified kinetic model for the degradation of 2-butanone in aerated aqueous solutions under steady-state gamma-radiolysis. Radiat. Phys. Chem. 58 (4), 341–356.
Xue, Q., Ran, Y., Tan, Y., Peacock, C.L., Du, H., 2019. Arsenite and arsenate binding to ferrihydrite organo-mineral coprecipitate: Implications for arsenic mobility and fate in natural environments. Chemosphere 224, 103–110.
Yakabuskie, P.A., Joseph, J.M., Keech, P., Botton, G.A., Guzonas, D., Wren, J.C., 2011. Iron oxyhydroxide colloid formation by gamma-radiolysis. Phys. Chem. Chem. Phys. 13 (15), 7198–7206.
Zachara, J.M., Kukkadapu, R.K., Fredrickson, J.K., Gorby, Y.A., Smith, S.C., 2002. Biomineralization of poorly crystalline Fe (III) oxides by dissimilatory metal reducing bacteria (DMRB). Geomicrobiol J. 19 (2), 179–207.
Zeng, Q., Huang, L., Ma, J., Zhu, Z., He, C., Shi, Q., Liu, W., Wang, X., Xia, Q., Dong, H., 2020. Bio-reduction of ferrihydrite-montmorillonite-organic matter complexes: effect of montmorillonite and fate of organic matter. Geochim. Cosmochim. Acta 276, 327–344.
Zhang, S., Cui, S., Gong, X., Chang, L., Jia, S., Yang, X., Wu, D., Zhang, X., 2016. Effects of gamma irradiation on soil biological communities and C and N pools in a clay loam soil. Appl. Soil Ecol. 108, 352–360.
Zhao, Q., Poulson, S.R., Obrist, D., Sumaila, S., Dynes, J.J., McBeth, J.M., Yang, Y., 2016. Iron-bound organic carbon in forest soils: quantification and characterization. Biogeosciences 13 (16), 4777–4788.
Zhao, Q., Adhikari, D., Huang, R., Patel, A., Wang, X., Tang, Y., Obrist, D., Roden, E.E., Yang, Y., 2017. Coupled dynamics of iron and iron-bound organic carbon in forest soils during anaerobic reduction. Chem. Geol. 464, 118–126.
Zhao, Q., Goto, R., Saito, T., Kobayashi, T., Sasaki, T., 2020. Effect of gamma-irradiation on complexation of humic substances with divalent calcium ion. Chemosphere 256, 127021.
Zhao, Q., Kobayashi, T., Saito, T., Sasaki, T., 2021. Gamma-irradiation-induced molecular-weight distribution and complexation affinity of humic acid with Cs(+), Sr(2+), and Eu(3). J. Hazard. Mater. 411, 125071.
Zhao, Q., Saito, T., Miyakawa, K., Sasamoto, H., Kobayashi, T., Sasaki, T., 2022a. Sorption of Cs(+) and Eu(3+) ions onto sedimentary rock in the presence of gamma-irradiated humic acid. J. Hazard. Mater. 428, 128211.
Zhao, Y., Moore, O.W., Xiao, K.-Q., Curti, L., Fariña, A.O., Banwart, S.A., Peacock, C.L., 2022b. The role and fate of organic carbon during aging of ferrihydrite. Geochim. Cosmochim. Acta 335, 339–355.